Proposal of an Experimental Search for μ-e Conversion in Nuclear Field at Sensitivity of 10^{-14} with Pulsed Proton Beam from RCS

M. Kinsho
JAERI, Tokai, Ibaraki, Japan

M. Ikegami, N. Kawamura, H. Kobayashi, H. Matsumoto,
T. Mibe, Y. Miyake, S. Mihara, H. Nishiguchi,
C. Ohomori, N. Saito, K. Shimomura, P. Strasser,
K. Yoshimura, M. Yoshii
KEK, Tsukuba, Ibaraki, Japan

M. Aoki[1]
Osaka University, Toyonaka, Osaka, Japan

T. Numao
TRIUMF, Vancouver, BC, Canada

D. Bryman
the University of British Columbia, Vancouver, BC, Canada

T. Taniguchi
Okayama University, Okayama, Japan

December 6, 2010

[1]Contact Person: aokim@phys.sci.osaka-u.ac.jp

Abstract

A new experiment searching for μ^--e^- conversion in nuclear field by fully utilizing the high-power pulsed proton beam available at J-PARC Material Life Science Facility (MLF) is proposed. A Monte Carlo simulation whose validity was confirmed by a test measurement indicates the muonic carbon atom formation rate in a muon target of J-PARC MLF being approximately 10^{10}/sec for 1 MW operation of a J-PARC booster (RCS). With this high formation rate of the muonic atoms, it is possible to perform a competitive search for μ^--e^- conversion in nuclear field.

The sensitivity of the measurement is 1.5×10^{-14} for silicon nuclei after 2×10^7 sec of the physics run if a H-line with large acceptance for 105-MeV/c electron is built in timely manner. The discovery potential of seeing the signal beyond the Standard Model is very high.

Contents

Chapter 1

Introduction

Lepton flavor invariance, which was a feature of the original Standard Model (SM) *a priori*, no longer holds since observations of neutrino oscillations have been firmly established[1]. This fact generally implies the existence of lepton-flavor violation in charged sector (CLFV) due to the mixing of neutrino flavors in the intermediate state. However the strength of such a process is suppressed by a GIM-like mechanism to the level of 10^{-60}[2] far beyond experimental accessibility. Because CLFV is practically still forbidden in the framework of neutrino-oscillation-extended SM, the experimental observation of CLFV would signal the existence of extraordinary new physics beyond the SM.

Numerous theoretical models describing the physics beyond the SM give predictions for the branching ratios of CLFV processes[3, 4, 5]. One such model, for example, is based on the combination of a supersymmetric model (SUSY) with a see-saw mechanism by right-handed heavy neutrino[6]. An interesting mass range of the right-handed heavy neutrino could be explored by CLFV experiments such as $\mu \rightarrow e\gamma$ and μ^--e^- conversion in nuclear field. Therefore experimental studies of these processes will certainly help to understand the structure of neutrino sector. Another model based on SUSY Grand Unified Theory[7, 8] also gives predictions for the branching ratio of $\mu \rightarrow e\gamma$ and μ^--e^- conversion in nuclear field. In this model, relatively a large top-quark mass results in rather larger radiative corrections to the slepton mass matrix, and the off-diagonal elements of the slepton mass matrix become sizable. As a result, smuon-selectron mixing in the intermediate state of the processes might induce CLFV, and calculations show the branching ratios being only a few orders of magnitude below the current experimental limits. Figure 1.1 shows an example of theoretical calculation for the decay branching ratio of $\mu \rightarrow e\gamma$ shown as a function of the muon anomalous magnetic dipole moment [9]. Appropriate assumptions on SUSY parameters and GUT relations, and constraints from B-physics experiments are applied in this calculation. The corresponding branching ratio for the μ^--e^- conversion is added on the right by assuming a dominant contribution by a photon exchange as explained below. It can be clearly seen that the μ^--e^- conversion above 10^{-14} is strongly favored in this scenario.

It is naively concluded that, if the $\mu \rightarrow e\gamma$ process exists, the μ^--e^- conversion in nuclear field should exist at the branching ratio of about $\alpha\times$ Br($\mu \rightarrow e\gamma$) where

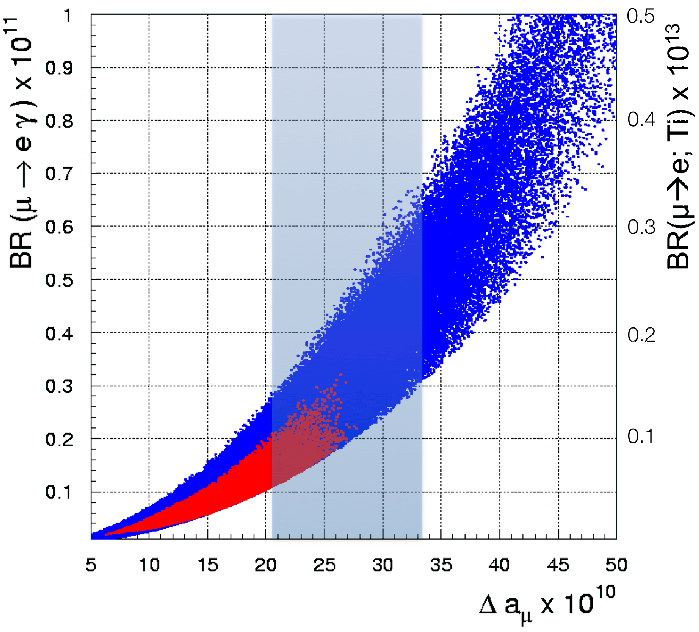

Figure 1.1: Expectation for B($\mu \rightarrow e\gamma$) vs. $\delta a_\mu = (g_\mu - g_\mu^{SM})/2$ with appropriate assumptions on SUSY parameters and GUT relations. Taken from [9]. The shaded area shows the recent measurement of Δa_μ[10].

α is the fine structure constant. This is because the photon exchange contributes to the μ^--e^- conversion in nuclear field as shown in Figure 1.2. There are, of course, potential differences in the type of interactions mediating $\mu \rightarrow e\gamma$ and μ^--e^- conversion in nuclear field; there is a possibility of other particle exchanges like Higgs bosons contributing to the μ^--e^- conversion in nuclear field[11]. In these cases, the branching ratio of the μ^--e^- conversion in nuclear field will be well larger than $\alpha\times$ Br($\mu \rightarrow e\gamma$). This means that performing searches for both processes (and others) is very important to maximize the discovery potential, and even after a discovery of CLFV in any process, other studies will stay complementary and provide indispensable information to understand the details of CLFV process and physics source behind that.

While experimental searches for CLFV processes have been extensively performed using many processes such as muon decays and reactions, tau decays, kaon decays, etc, muons have provided the highest sensitivity. Figure 1.3 shows a history of experimental limits ever achieved for different processes including leptons; Table 1.1 shows the current limits on CLFV from several muon experiments. The reason why muons are suited for CLFV search experiments, as seen in the figure, can be simply explained by two features: higher muon production rate and the long muon life time. The current best limit of the μ^--e^- conversion in nuclear field is set by the SINDRUM II collaboration at 7×10^{-13} using a gold target [17]. A leading experiment searching for $\mu^+ \rightarrow e^+\gamma$ at the level of 10^{-13} is on-going at Paul Scherrer Institute (MEG) where the world's most intense DC muon beam is available. The MEG experiment

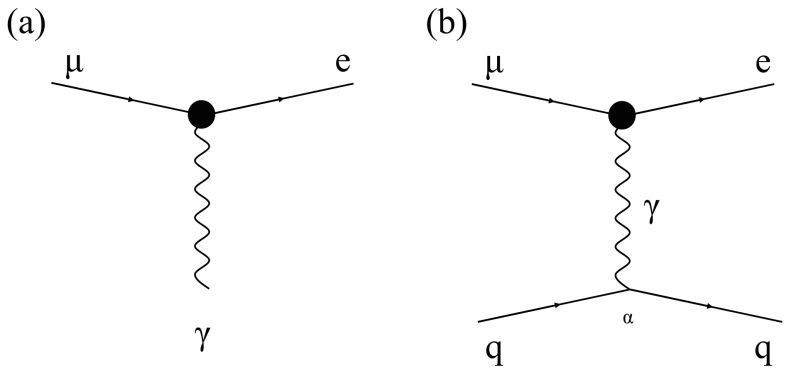

Figure 1.2: LFV processes of the muon. (a) $\mu \rightarrow e\gamma$ and (b) μ^--e^- conversion in nuclear field.

Table 1.1: Present limits on CLFV from muon experiments.

Reaction	Present limit	Reference
$\mu^+ \rightarrow e^+\gamma$	$< 1.2 \times 10^{-11}$	[13]
$\mu^+ \rightarrow e^+e^+e^-$	$< 1.0 \times 10^{-12}$	[14]
$\mu^- + \mathrm{Ti} \rightarrow e^- + \mathrm{Ti}$	$< 4.3 \times 10^{-12}$	[15]
	$(< 6.1 \times 10^{-13})$	[16] unpublished
$\mu^- + \mathrm{Au} \rightarrow e^- + \mathrm{Au}$	$< 7 \times 10^{-13}$	[17]

has published first result in 2010 [18] and new result with more statistics to go beyond the current experimental limit is expected in near future [19]. Based on the expected sensitivity of the experiment and theoretical predictions as introduced above, this experiment may have a real chance of a discovery. Even when the MEG would not find any signal, it is true that the MEG result will restrict more strongly the new physics beyond the SM.

There are several muon experiments planned with equivalent sensitivity to or better than the SINDRUM II and MEG experiments. Among these, μ^--e^- conversion in nuclear field i.e. the neutrinoless muon capture reaction μ^- + A(N,Z) $\rightarrow$ e^- + A(N,Z) is highly favorable for future study because a wide range of new processes involving both quarks and leptons may contribute to make this reaction sizable. Note that the search for μ^--e^- conversion in nuclear field is experimentally advantageous compared to the $\mu \rightarrow e\gamma$ search because the signature involves only a single mono-energetic electron for which backgrounds are expected to be quite low. Furthermore the experiment does not suffer from random coincidence backgrounds as in the case of the $\mu \rightarrow e\gamma$ search. Figure 1.4 shows an example prediction of the decay branching ratios of $\mu \rightarrow e\gamma$ and μ^--e^- conversion in Little Higgs model. In this model, unlike the SUSY case, box and penguin diagrams give leading contribution to the μ^--e^- conversion amplitude, resulting in a favored region of BR($\mu \rightarrow e$;N)$> 10^{-14}$ and a

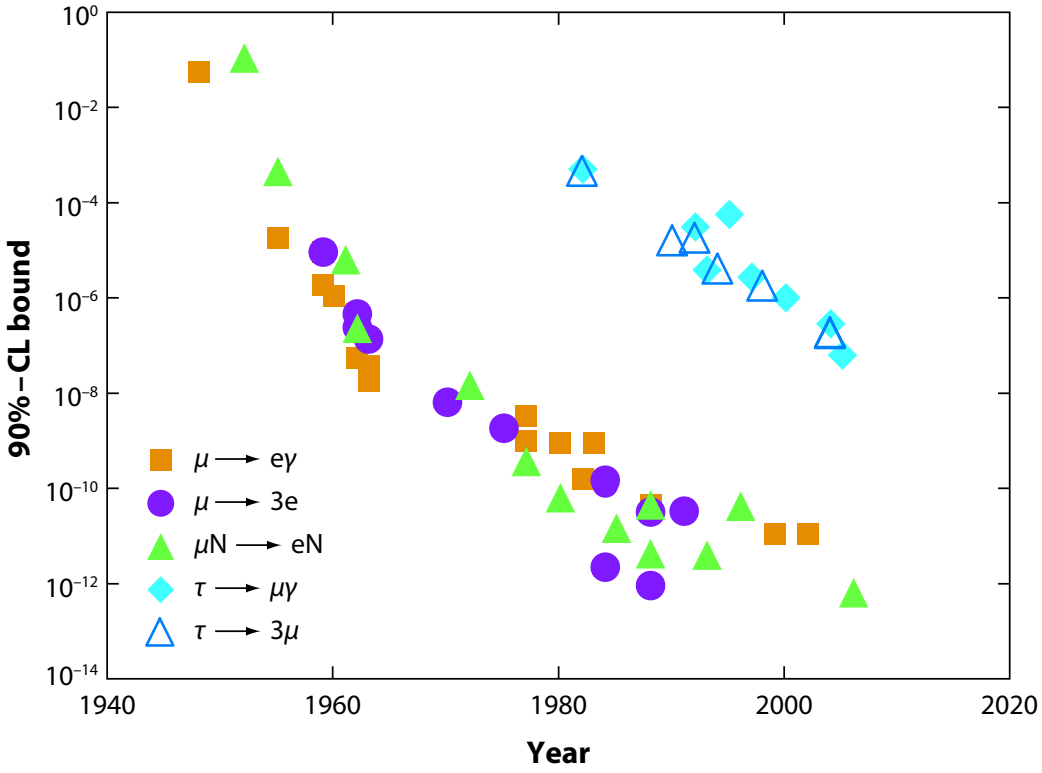

Figure 1.3: History of experimental limit improvement of CLFV processes [12].

relation of the branching ratios of $\mathrm{Br}(\mu \to e;\ \mathrm{N}) \sim \mathrm{Br}(\mu \to e\gamma)$.

Two major new experimental enterprises aiming to search for $\mu^- + \mathrm{Al} \to e^- + \mathrm{Al}$ at a level of 10^{-16} have been proposed at J-PARC (COMET[21]) and Fermilab (Mu2e[22]). These experiments are really challenging projects and require extraordinary financial and technical investments, resulting in a decade to mount and operate the experiments. In particular realization of the necessary pulsed-proton beam for these experiments requires tremendous effort. If the required performance of the beam were not realized, those experiments would not be able to reach their target sensitivity. In these circumstances an opportunity exists to improve the sensitivity with modest cost and a near-term time scale at the J-PARC MLF where the world's most intense pulsed-muon beam is available.

We propose to search for the μ^--e^- conversion in nuclear field at J-PARC MLF with a sensitivity of 10^{-14}, two orders of magnitude below current limits. The experiment will be conducted by using the muon beam provided at MLF. Our intention is to realize the experiment in a timely manner by making a use of the MLF muon target system as a muon-stopping target to form muonic atoms, and the muon beam line as a detector-rate suppressor to make the detector functional under very high rate of the muonic atom formation.

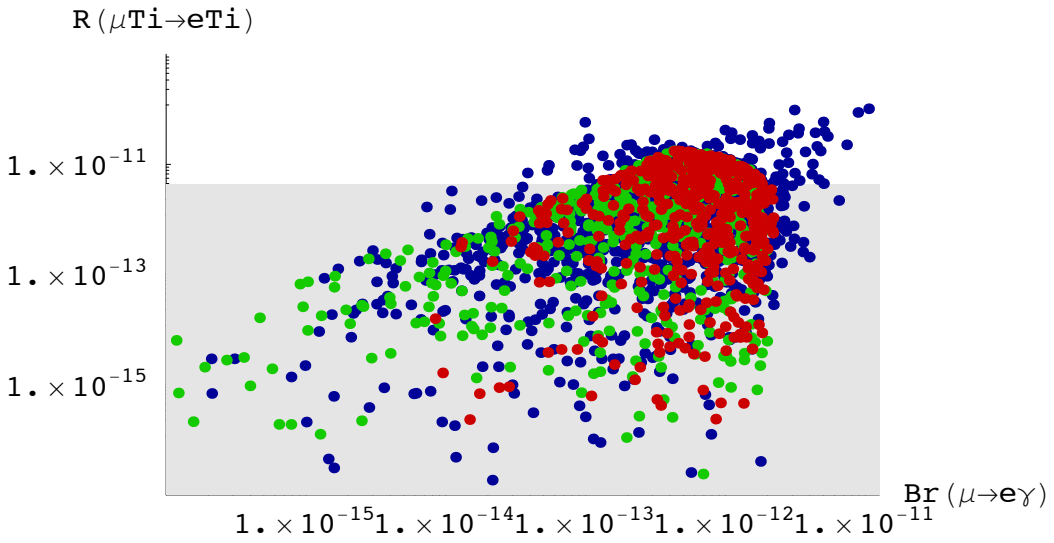

Figure 1.4: Prediction of the branching ratio of μ^--e^- conversion and $\mu \rightarrow e\gamma$ in Little Higgs model [20].

A CLFV signal may be seen in near future by experiments which improve the current limits. It is conceivable that the CLFV signal lies waiting to be discovered right under the current limit. A new experiment searching for μ^--e^- conversion in nuclear field at the 10^{-14} level would be a highly competitive addition to the field especially for the case when the MEG discovers the signal at 10^{-12}.

Chapter 2

Overview

The key idea of the proposed experiment is to utilize the muonic atom that formed in the production target itself, and use the ordinary secondary beamline to extract electrons coming from $\mu^- + \mathrm{A(N,Z)} \to e^- + \mathrm{A(N,Z)}$ reaction in the production target.

2.1 Experimental Apparatus

The experimental apparatus is divided into several components as shown below.

Target Region A part of low-energy pions produced by the primary proton beam will decay in flight to muons only within a few centimeters after the production. Some of muons from the pion decay-in-flight will stop in the production target itself.

The muonic atom yield in the production target will be 10^{10}/sec for 1-MW operation of the J-PARC Rapid-Cycle-Synchrotron booster (RCS). The material of the production target will be silicon carbide so that 70% of μ^- can be atomic-captured by silicon atom.

Secondary Beamline An ordinary secondary beamline will be used for extracting 105-MeV/c electrons from the target. There are huge amount of Michel electrons and positron from $\mu^\pm$ in the target, but most of them are blocked by the secondary beamline. In order to increase the statistical significance, the beamline should transport the 105-MeV/c electrons with high transport efficiency.

Kicker System There will be a huge number of electrons promptly produced by the primary proton hitting the production target. One of such production process would be $p + N \to \pi^0 N'$, $\pi^0 \to \gamma\gamma$ and $\gamma \to e^+e^-$ in material, for example. The rate of such prompt electrons is estimated to be 10^7 per proton pulse. If these electrons hit the detector, it will be blinded for while and will miss the chance to detect the delayed signal electrons. The kicker system is used to reduce the rate of the prompt electrons by factor 10^3–10^4.

Detector The detector system should measure the electron momentum with 0.5% (rms) of resolution in order to distinguish the signal from the decay-in-orbit backgrounds. It also has to withstand the prompt electrons up to 10^4 per pulse. Since the size of electron beam is about 200×200 mm, the instantaneous rate of the prompt electrons is about 0.25 MHz per mm^2. It is very high but still within the reach of the existing technology of the gas wire chamber.

Plastic scintillation counters can be operational even after 10^3 of prompt burst if the gain of photomultipliers is lowered by changing the high voltage of grid and dynodes (gating-grid PMT) during the prompt burst.

2.1.1 Muonic Atom Formation in a Muon Production Target

When a high intensity proton beam from the MLF hits a production target, a huge number of pions is copiously produced. The energy distribution of these pions shows a very diverse spectrum ranging from very low energy to high energy, and the production yield of low energy pions is quite large. Some of those low energy pions stop in the production target itself and decay to muons by $\pi^+ \to \mu^+\nu_\mu$ decays. Since the energy of those decay-at-rest muons is only 4 MeV and the range is not longer than 0.1 g/mm^2, most of those muons do not emerge out of the production target. However, muons from the pions stopped in the very thin surface layer of the production target can emerge out of the target. This is the mechanism of how "surface muons" are produced. Since the yield of low energy pions is very large, the yield of surface muons is also large. For example, the typical yield is about 10^8/sec at the PSI πE5 beamline (150 msr, $\Delta p/p = 10\%$).

The probability of 4 MeV muons emerging out of the muon target in J-PARC MLF is calculated to be only a level of 10^{-3}[23]. Assuming the acceptance of typical beamline to be 10^{-2}, the number of μ^+ stopped in the production target should be a level of 10^{13}/sec or more.

It is well known that the "surface μ^-" does not exist because the parent particle π^- is promptly absorbed by the target nucleus after it stops and does not decay to muons. However, low energy pions in flight will decay and produce low energy μ^-s. These muons are called "cloud μ^-", and it is known by experience that the yield of cloud μ^- is about 2% of the surface μ^+ when observed by a typical beam line.

Some fraction of the low energy cloud μ^- produced around the target stops in the target. Then, those μ^- will from muonic atoms. By taking into account the μ^+ stopping rate ($\sim 10^{13}$/sec), the ratio of cloud-μ^- to surface-μ^+ ($\sim$2%), and material near the target, the yield of muonic atom formation at a level of 10^{10}/sec, could be anticipated. The actual yield of the muonic atom should depends on the geometry of target region. The details of the muonic atom formation rate in the muon target at MLF will be discussed in Chapter 3.

2.1.2 μ-e Electrons from the Muon Production Target

Once muonic atoms are formed in the production target, one of following processes will occur:

1. Muon decay in orbit (DIO): $\mu^- \to e^- \nu_\mu \overline{\nu}_e$,
2. Muon capture (MC): μ^- + A(N,Z) $\to \nu_\mu$ + A'(N,Z-1) or
3. μ-e conversion in nuclear field (MEC): μ^- + A(N,Z) $\to e^-$ + A(N,Z).

The former two processes are well described within the SM, but the last process, MEC, is a CLFV process that the experiment described here is searching for. Since the overlap of μ^- wave function and the target nuclei causes both MEC and MC processes, the strength of the MEC process is normalized to that of MC:

$$\mathrm{BR}(\mu^- + \mathrm{A(N,Z)} \to e^- + \mathrm{A(N,Z)}) \equiv \frac{\Gamma[\mu^- + \mathrm{A(N,Z)} \to e^- + \mathrm{A(N,Z)}]}{\Gamma[\mu^- + \mathrm{A(N,Z)} \to \nu_\mu + \mathrm{A'(N,Z\text{-}1)}]} . \quad (2.1)$$

Muons those undergo DIO process do not contribute to MEC search, but just be wasted and produce the backgrounds. Since the fraction of DIO becomes less as atomic number of target nuclei increases, heavy nuclei is better than light one from that point of view. For examples, the fraction of MC is only 8% for carbon, and almost 70% for silicon.

Now, both DIO and MEC processes emit electrons. The electron from MEC is mono-energetic at E_{max}, where E_{max} is given as:

$$E_\mu = E_{\mathrm{max}} + \frac{E_{\mathrm{max}}^2}{2M_A} , \quad (2.2)$$

$$E_\mu = m_\mu - B_\mu . \quad (2.3)$$

M_A is the mass of the target nucleus, m_μ is a mass of muon and B_μ is a binding energy of μ^- in the Coulomb potential of the muonic atomic. The E_{max} is 105.1 MeV and 105.0 MeV for $^{12}_{6}$C and $^{28}_{14}$Si, respectively. On the other hand, the electron energy from DIO shows continuous spectrum from 0 MeV to E_{max}, and the spectrum falls steeply above $m_\mu/2$. The spectrum shape near E_{max} is very steep and known to be approximated by $(E_{\mathrm{max}} - E_e)^5$[24]. Therefore, the contamination of DIO electrons to signal electrons can be suppressed by raising the lower energy threshold in the signal-electron detection.

The amount of DIO near the end-point energy is less for the light nuclei if the process is normalized to the total number of DIO[25]. However, if it is normalized to the total μ^- atomic-captured, then it becomes much larger in the light nuclei since the fraction of μ^- going DIO overwhelm that of MEC. For examples, the fraction of DIO per MC at $E_e > 102$ MeV/c is 5.5×10^{-14} for carbon and 1.1×10^{-14} for aluminum. This fact actually affects the selection of proper material as the muon stopping target, thus the optimization of the target region. The details will be described in Chapter 3.

The second feature of MEC electron is its timing. Since MEC electrons are emitted by μ^- bound in material, they show an exponential time spectrum, $e^{-t/\tau}$, where τ is a μ^- lifetime in the material. Since μ^- disappears through either DIO or MC, the lifetime becomes shorter than the life time in free space where MC does not contribute. The μ^- lifetime in carbon is 2.03 μsec, and that in silicon is 0.76 μsec.

It is noteworthy that they are indeed shorter than the lifetime in free space but still longer than the time scale of electromagnetic and strong interactions.

There are many sources of 105-MeV electrons from the production target other than DIO, but all of them are from either electromagnetic interactions or strong interactions followed by electromagnetic interactions. One example is $\pi^0 \to \gamma\gamma$ followed by γ converting to e^-e^+. Those electrons are promptly emitted after proton hitting the target. This contrasts with the delayed emission of electrons from μ^- in material. Actually, the source of the delayed electrons whose time scale is the order of the muon life time is only from muon decay. Because of this, if there is any electron emission with energy $E_{\rm max}$ delayed by μsec order after proton hitting the target, it is a signal of MEC.

The potential source of background may be from late arriving protons hitting the production target. In order to suppress those kind of backgrounds, the late-arriving protons should be suppressed as less as 10^{-17} of on-timing protons. This suppression factor is certainly extremely small, but there is no reason why it can not be achieved in the fast extraction from J-PARC RCS. This will be discussed in Chapter 7.

2.1.3 Detection of μ-e Electrons

The μ-e electrons produced in the muon production target can be extracted by a secondary beamline. This secondary beamline has the following functions:

1. to extract high momentum 105-MeV electrons

2. with large solid angle to increase the physics sensitivity,

3. suppress the DIO electrons, and

4. eliminate the prompt burst by a kicker system.

An example of the beam line is a D-line currently exist in J-PARC MLF Muon Science Facility. It can be operated up to 120 MeV/c, which satisfies the 1st requirement above, and the geometrical acceptance is about 30 msr[1]. The D-line consists of three dipole magnets, and almost completely eliminate low momentum particles. A pulse kicker system will be installed at the end of 2010.

Although it is possible to perform the experiment at D-line, the physics sensitivity is limited by the smallness of overall transport efficiencies of the beam line. Since it is critically important to increase the acceptance of beamline, a new beamline using the High-Momentum Decay Muon port, H-line, is considered. The physics sensitivity at the new beam line could be almost an order of magnitude better than the measurement at the D-line.

[1]for the point-like source, but much smaller for the finite-sized source

Table 2.1: Target configurations.

	As it is	wide carbon	wide SiC
Muon Production Target Material	C	C	SiC
Muon-Stopping Nuclei	C	C	Si
$N_{\mu\text{-stop}}$ ($\times 10^9$/proton)	10	15	15
f_{C}	1	1.0	0.7
f_{MC}	0.08	0.08	0.66
ε(Time Window)	0.75	0.75	0.49
FoM	0.6	0.9	3.4

Table 2.2: Beamline configurations.

	D-line	D-line (updated)	H-line
Note	—	new DSEPTUM	—
Geometrical Acceptance	30 msr	30 msr	110 msr
Transmission Efficiency	30%	60%	100%
Average Acceptance	10 msr	18 msr	110 msr

2.2 Experimental Configurations

The measurement can be performed in various configuration sets, they are different in the total cost, sensitivity and schedule. The configuration can be chosen by a combination of the target configuration and beamline selection.

2.2.1 Target Configuration

Table 2.1 summarizes three typical configurations of the target region. The highest figure-of-merit is obtained when the material of a currently-planned rotation carbon target is replaced with Silicon Carbide (SiC), and the outer radius is extended by 20 mm.

2.2.2 Beamline Selection

As it will be discussed in details in Chapter 4 and 5, the overall acceptance is almost one order of magnitude higher in H-line. Table 2.2 shows three potential configurations of the beamline.

2.2.3 Figure of Merit

Taking the combination of the target merit and beamline merit, the less sensitive option is to use a rotation carbon target with the current D-line without any modi-

fications. The single event sensitivity (S.E.S) after running 2×10^7 s is 6.5×10^{-13}, which is almost the same to the current upper limit given by SINDRUM-II[17]. However, in case of not seeing any events, the upper limit will be given by $2.3 \times$ S.E.S, and it will be worse than the SINDRUM-II gold measurement.

The most sensitive option is to use the SiC rotation target with H-line. The S.E.S will be 1.5×10^{-14} after running 2×10^7 s of data taking. The construction of a new H-line is necessasry.

Chapter 3

Target Region

In the target region, the following three processes will be taken place:

- π^- are copiously produced by primary proton beam,
- π^- decay to μ^- in flight, and
- μ^- stop in a muon stopping material,

where the muon stopping material is the primary proton target itself in our case.

The best design of the target region is basically the one that gives the highest yield of the muonic atom, but the beamline acceptance of the e^- from MEC should be also taken into account. For this purpose, the figure of merit of the target design is defined as:

$$\text{FoM} \;=\; R_{\pi^-} \times f_{\pi^- \to \mu^- \text{stop}} \times f_{\text{C}} \times f_{\text{MC}} \times f_{\mu-e} \times A_{\mu-e}\,, \tag{3.1}$$

where R_{π^-} is π^- production rate, $f_{\pi^- \to \mu^- \text{stop}}$ is a probability of π^- that produce μ^- stopping in the production target, f_{C} is a probability of μ^- that atomic-captured by the atom of interest, f_{MC} is a fraction of μ^- that goes to the muon capture process, $f_{\mu-e}$ is the relative strength of the μ-e conversion process, and $A_{\mu-e}$ is the acceptance for 105-MeV/c electrons. The estimation of those factors and the optimization of the FoM will be described in this chapter.

3.1 Target Assemble in the Muon Science Facility

A muon production target in the Muon Science Facility, MLF at J-PARC, is made of an isotropic graphite (IG-43) with a thickness of 20 mm. The thickness is limited so that the loss of the primary proton should be less than 10% for the neutron facility located downstream of the muon production target. Figure 3.1 shows image of the muon production target currently in use. The graphite is shaped as a disk, and the diameter is 70 mm. The edge of the graphite disk is surrounded by a frame made of copper with stainless steel tubes buried in for the water cooling. The heat load will be 3.3 kW and 0.6 kW in the graphite and in the frame, respectively, when the

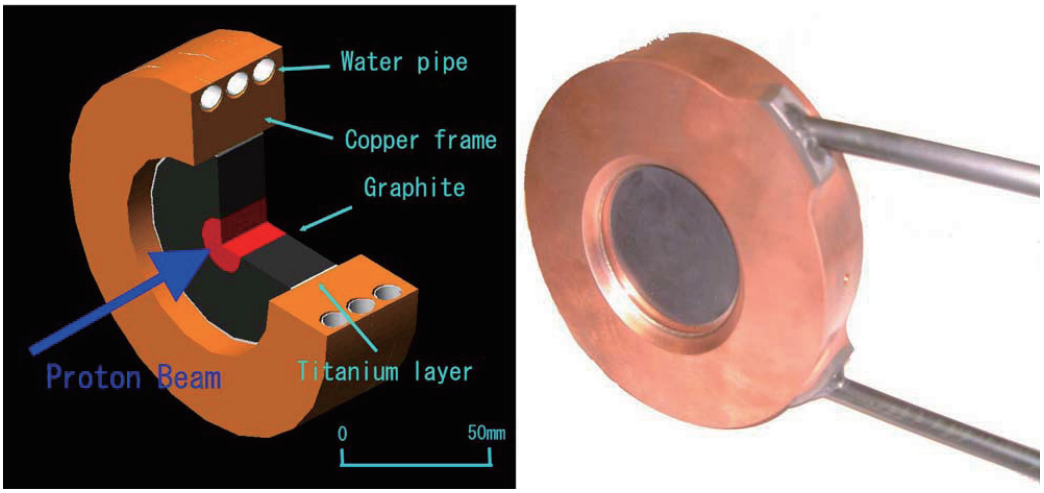

Figure 3.1: The left panel shows a schematic drawing of the target assembly currently in use. The right panel shows a picture of the target. This figure was taken from [26].

primary proton beam power becomes 1 MW[26]. The temperature of the center of the graphite disk will be 1500°C. The radiation dose at the center of the graphite will be 1 dpa/year maximum[27].

The graphite IG-43 will shrink by 1% per 1dpa of radiation, and it causes extra tensor force in the graphite. Therefore, this muon production target should be replaced in every half year under 1 MW operation. In order to overcome this difficulty, another design of the target is currently underway. Figure 3.2 shows schematic drawing of the new target. graphite ring is attached around a rim, and the ring will be rotated at 5 r.p.m. The heat load to the graphite ring will be 4 kW under 1-MW RCS operation, and the target ring is cooled by heat radiation. The size of the graphite ring is 350 mm outer diameter, 250 mm inner diameter and 20 mm thickness. The expected maximum temperature of the graphite is 1000 K. The life time of the rotating target is designed to be 10 years.

The new target will be installed in the muon facility within a couple of years before the life time of the current fixed target comes to the end. The proposed experiment will be in operation with the rotation target.

3.2 Pion Production Rate

If the pion production cross section is well known, the factor R_{π^-} can be easily calculated once the primary proton energy, power and the material and the geometry of the production target are defined. The difficulty of the calculation actually lies down the uncertainly of the cross section. In order to minimize the uncertainly, the R_{π^-} was estimated by using three different methods, and double-checked with an actual measurement.

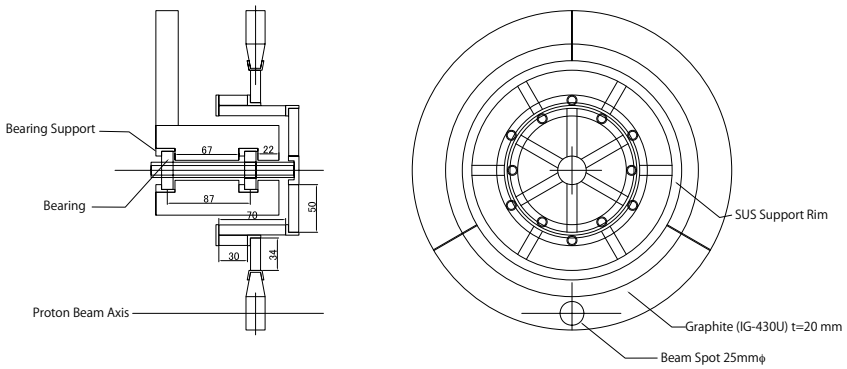

Figure 3.2: The schematic design of the rotation-type muon target, which will replace the current fixed-type target.

3.2.1 Estimate of the Pion Production by using Be Data

A measured pion production cross section by 2.9 GeV proton on a Be target was reported by P.A. Pirone *et al.*[28]. Figure 3.3 shows the pion production cross section from their study. Solid curves in the figure are from an empirical formula as follows:

$$\frac{d^2\sigma}{dEd\Omega}[\mu\text{barn/MeV}\cdot\text{sr}] = \frac{80\times 40aE}{(33+1200a+40aE)(1+\exp(40aE/60-2))(1+\exp((E-1000)/200))} \quad (3.2)$$

where

$$a = 0.001 + 0.02\tan\theta_1\,, \quad (3.3)$$

$$\theta_1 = \begin{cases} \dfrac{\theta}{1.5} & (\theta < 90^\circ) \\ 0.32(\theta - 90^\circ) + 60^\circ & (\theta > 90^\circ)\,, \end{cases} \quad (3.4)$$

and E is in MeV. This formula was introduced by Ishida in his surface muon yield calculation[23] for the design of the MLF Muon Facility. By integrating this cross section for all directions and up to 400 MeV/c of pion momentum, the total cross section becomes 50 mb. This corresponds to the total pion production rate being 2×10^{13} for 1 MW of proton beam on the muon target at MLF (20 mm thickness graphite).

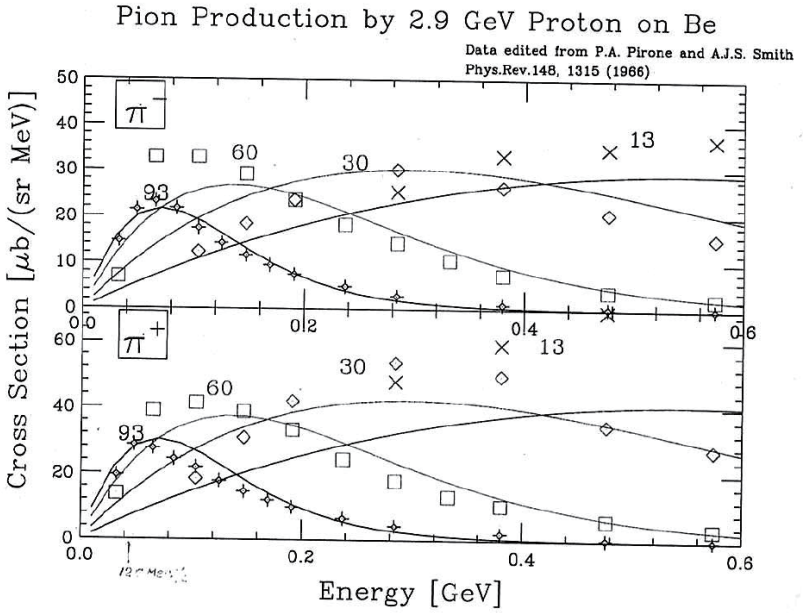

Figure 3.3: Pion production cross section by 2.9 GeV proton on Be target.

3.2.2 Estimate of the Pion Production by using HARP Data

HARP is an experiment measuring charged pion production for various proton energies and materials. The cross sections of pion production by 3 GeV/c–12 GeV/c protons on carbon target are available[29]. The double-differential cross section of π^- production by 3 GeV/c on carbon for $0.95 < \theta < 1.15$ and 0.10 GeV/$c < p_\pi <$ 0.15 GeV/c is

$$\frac{d^2\sigma}{dpd\theta} = 0.038 \pm 0.013\,\mathrm{barn/GeV}/c \cdot \mathrm{rad} \tag{3.5}$$

Integration over $0.95 < \theta < 1.15$ and 0.10 GeV/$c < p_\pi <$ 0.15 GeV/c gives $\sigma = 0.4 \pm 0.1$ mb. The pion production cross section from Eq. (3.2) for the same kinetic region is 0.9 mb. They are consistent within factor two.

3.2.3 Estimate of the Pion Production by Geant4

Geant4 is a Mote Carlo simulation code to estimate interactions and transports of particles in matter[30]. In the Geant4, hadron interaction is not built in, and user has to prepare for the hadron interaction code. There are many different hadron codes available, and the choice depends on the purpose of the application. QGSP_BERT_HP is one of such codes, and was reported to be the best for pions and protons at low energy (< 0.7 GeV)[31]. Other report stats that QGSP_BERT is not the best but usable[32], but QGSP_BERT_HP is an improved version of QGSP_BERT and this statement may be no longer valid.

In order to evaluate the pion production rate, A Monte Carlo calculation using Geant4 with QGSP_BERT_HP was performed. Figure 3.4–3.5 show the pion momentum spectra at birth by 3-GeV protons on the carbon target, displayed in different angle bins for π^+ and π^-, respectively. The result of HARP measurements are also shown in the plots. The result from QGSP_BERT_HP shows fairly good agreement with HARP data. The disagreements are larger in forward region, especially in higher momentum region $p > 200$ MeV/c. However, as shown in the next section, the momentum of negative pions that produce negative muons from decay-in-flight and the muons stop in the production target itself is mostly less than 200 MeV/c. In that momentum region, HARP and QGSP_BERT_HP show very good agreement.

Based on this result, we decided to use the Geant4 with QGSP_BERT_HP for the following studies. The difference between HARP result and Be data estimation is not understood, but the estimation with Geant4, which is consistent with HARP, gives lower yield than the Be data estimation. Our estimation is very unlikely to be overestimate.

3.3 Stopped Muon Production Efficiency

The factor $f_{\pi^- \to \mu^- \mathrm{stop}}$ is mostly determined by the geometrical configuration of the target section, such as the target shape, size, thickness. It also mutually depends on the direction and energy of the produced pions. Therefore, The Monte Carlo calculation using Geant4 was performed to estimate $R_{\pi^-} \times f_{\pi^- \to \mu^- \mathrm{stop}}$ at once. The hadron code used for the estimation was QGSP_BERT_HP as was explained previously. Figure 3.6 shows the production momentum spectrum of π^- which produce μ^- stopping in the production target. Only those low momentum pions can decay in flight to low energy muons, where the muons can stop in the production target. The results are $R_{\pi^-} \times f_{\pi^- \to \mu^- \mathrm{stop}} = 7.6 \times 10^9$/sec in the Graphite disk of the fixed-type muon production target for 1 MW operation of J-PARC RCS. It will be $R_{\pi^-} \times f_{\pi^- \to \mu^- \mathrm{stop}} = 10 \times 10^9$/sec in the graphite ring of the rotation-type target for 1 MW operation. Figure 3.7 shows 3D model of the rotation target implemented in Geant4. The outer rim(20 mm^t, inner radius 132.5 mm, outer radius 167.5 mm) is made of graphite and the primary proton hit 17.5 mm from the lower edge of the outer rim. The size of the proton beam is 25 mm diameter.

In the D-line, size of source should be smaller than 20 mm radius. Any particles coming from the outside of this area would not be transported down to the detector area. In the H-line, it will be larger than that of D-line and will be 30 mm radius. Therefore, the target material should cover the 30-mm radius area around the secondary beamline axis in order to maximize the experimental sensitivity. In order to estimate the effect of the target size, the Geant4 calculation was also performed with a slightly wider size of the graphite ring: outer radius 187.5 mm, which corresponds to 35 mm of source radius, and large enough to cover the source area of the H-line. Table 3.1 shows the results of these calculations. The yield of the muonic carbon atom is larger in the rotation target since the volume of the graphite ring is larger than the volume of graphite in the fixed-type target. Please note that this large

Table 3.1: Yields of muonic atoms produced by 1MW of 3-GeV proton beam hitting the muon production target.

Configuration	$R_{\pi^-} \times f_{\pi^- \to \mu^- \mathrm{stop}}$ (/s·MW)
The present fixed target	7.6×10^9
The new rotation target	10×10^9
Wide rotation target	15×10^9

yield does not instantly means the increase of the physics sensitivity. Some of muonic atoms are outside of the secondary beamline acceptance. The final sensitivity should be compared after taking into account of the secondary beamline acceptance.

3.3.1 Measurement of Muonic Carbon Atom Formation Rate

The pion production rates calculated by using two data sets (Piroue and HARP) and that calculated with the QGSP_BERT_HP model of Geant4 show fairly good agreement. However, the cross section data do not completely cover whole the kinematics region, and the QGSP_BERT_HP model is just a model with some uncertainty in its precision at the low energy region. Therefore, a test experiment to measure the muonic atom formation rate in the fixed-type Muon Target was performed at Area D2 of D-line in November 2009[1]. Figure 3.8 shows a typical time spectrum of delayed electrons with the beamline momentum setting being 40 MeV/c at D-line. The shape of time spectrum was fit to $Ae^{-\frac{t}{\tau}}$, by using MINUIT, and the result is $\tau = 2.094 \pm 0.005$ μs. According to the Geant4 Monte Carlo study, this time spectrum should composed of two components: exponential decay with $\tau_1 = 2.0$ μs and $\tau_2 = 2.2$ μs. The former comes from the decay of μ^- in a carbon atom. The latter comes from μ^+ decay in the carbon target followed by the Bhabha scattering ($e^+ + e^- \to e^+ + e^-$) off the electrons in material. Since the yield of μ^+ decay is more than 500 times larger than μ^-, the effect of the Bhabha scattered e^- is not negligible. If the statistics of the plot was much more, then these two components could be separated. The percentage of the Bhabha scattered e^- is estimated to be 20% by Geant4 Monte Carlo. Nonetheless, the observed time spectrum is fairly consistent with the μ^- life time in carbon. The rate of the muonic carbon atom formation obtained from this result with the correction of D-line transmission acceptance is 0.7×10^9/sec for 120 kW operation of MLF at the time of measurement. By scaling up with the primary beam power, it corresponds to 6×10^9/sec for 1 MW operation, and it is consistent with the estimation by the Geant4 within 20–30%. Therefore, the estimation of the muonic carbon atom formation rate from Geant4 with QGSP_BERT_HP is quite reliable within 30% of accuracy.

[1] A similar measurement was also performed at TRIUMF in 2008[33]

3.4 Muon Capture and μ-e Conversion Strength

When μ^- stops in the material, it will be captured by the Coulomb potential of the nuclei, and promptly falling down to the 1S state of the atomic orbit. This process is called "atomic capture of negative muon". If the material consists of a single type of atom, then the fraction of the atomic capture in the atom is 100% ($f_{\rm C} = 1$). However, if the material consists of several different atoms, μ^-'s are divided among these atoms with the probability scaling to the product of the atomic number (Z) and the number density of the atom. This is so called Fermi-Teller Z law[34]. For examples, if the material is silicon carbide (SiC), the fraction of μ^- trapped in Silicon atoms is $14/(14+6) = 0.7$, and that of carbon atoms is 0.3. It is known that the accuracy of the Fermi-Teller Z law is very rough, and $f_{\rm C}$ for Si would be even higher[35].

Once the μ^- is atomic captured, it will potentially go the following three processes:

1. Muon decay in orbit (DIO): $\mu^- \to e^- \nu_\mu \overline{\nu}_e$,
2. Muon capture (MC): $\mu^- + {\rm A(N,Z)} \to \nu_\mu + {\rm A'(N,Z\text{-}1)}$ or
3. μ-e conversion (MEC): $\mu^- + {\rm A(N,Z)} \to e^- + {\rm A(N,Z)}$.

The μ^-s went for DIO process do not contribute the measurement of MEC since MEC is only mediated by the contact interaction with nuclei. This is why the MEC branching ratio is defined as the ratio to the MC strength. In order to take into account of this fact, the figure of merit of the measurement has to be normalized by $f_{\rm MC}$. It strongly depends on the atomic number Z especially in the light nuclei.

In the μ-e conversion in nuclear field, nucleons in the target nucleus contributes the process in a coherent way, and the amplitude of the process strongly depends on the nuclear configuration, mostly the number and distribution of neutrons and protons. Therefore, the sensitivities to the new physics are different for different atomic numbers in the μ-e conversion[37, 38]. This effect can be taken into account by the parameter $f_{\mu-e}$. Table 3.2 shows $f_{\rm C}$, $f_{\rm MC}$ and $f_{\mu-e}$ for different materials[39, 40]. However, please note that the parameter $f_{\mu-e}$ shown in the table is model dependent. If we remove any theoretical prejudices, there is no concrete estimate to the parameter $f_{\mu-e}$. It even can be accidentally zero for particular Z[41]. From that point of view, it is very important to perform the experiment for several different Z.

The triple products $f_{\rm C} \times f_{\rm MC} \times f_{\mu-e}$ gives rough guide on the physics sensitivity per muonic atom. The number of carbon is almost one order of magnitude less than the both number of silicon carbide and aluminum. It is preferable to design the target region so that the muonic atoms are formed in silicon or aluminum rather than carbon.

3.5 Silicon Carbide Target

In order to maximize the physics sensitivity, we are considering to replace the current carbon target with a silicon-carbide target. The silicon carbide is the only chemical

Table 3.2: μ^- capture rate and lifetime for different materials.

	C	Al	Ti	Pb	Si(SiC)
Atomic Number	6	13	22	82	14+6
Capture Rate ($\times 10^6\,\mathrm{s}^{-1}$)	0.039	0.68	2.6	15	0.87(Si)
Lifetime (μs)	2.0	0.88	0.33	0.082	0.76
f_{C}	1	1	1	1	0.7
f_{MC}	0.08	0.60	0.85	0.97	0.66
$f_{\mu-e}$[37]	0.7	1	1.7	1.15	1
$f_{\mathrm{C}} \times f_{\mathrm{MC}} \times f_{\mu-e}$	0.056	0.60	1.45	1.12	0.46

Table 3.3: Typical Properties of Graphite and SiC. The purpose of this table is to impress the excellent properties of SiC. It is note worth that the details of the properties depends on how the materials are produced.

	Graphite (IG43)	SiC SiC	SiC+Si SiC+Si	SiC/SiC composite
Density (g/cm^3)	1.82	3.1	2.9	2.5
Flexural Strength (MPa)	54	580	250	
Young's modulus (GPa)	10.8	406	314	
CTE† ($\times 10^{-6}$/K)	4	4	4	†
Thermal conductivity (W/m·K)	140	130	150	
Thermal shock resistance (K)		550	450	
Neutron Irradiation (3.5dpa)[42]				
Swelling/Shrinkage	-2%			1%
Drop of Flexural Strength				$< 10\%$

Coefficient of thermal expansion

compound of carbon and silicon. It is an excellent abrasive and has been produced for over one hundred years. Today, it has been developed into a high quality ceramic with very good mechanical properties, and the application to many high-performance demanded fields are developed, such as nuclear fusion reactor, space applications, and so on.

Table 3.3 compares material properties of silicon carbide and graphite. Silicon carbide is not attacked by any acids or alkalies up to 800°C, and forms a protective silicon oxide coating at 1200°C in air, and able to be used up to 1600°C. The high thermal conductivity couples with low thermal expansion and high strength give this material exceptional thermal shock resistant qualities. The mechanical strength of a SiC/SiC composite show no degradation up to 3.5 dpa of neutron irradiation[42].

The draw back of using the silicon carbide as the production target is that it could increase the proton loss in the target. If the thickness is reduced to control the proton

loss being less than 10%, then the muonic atom yield would be decreased. The detail design of the silicon-carbide target is on-going.

3.6 Acceptance of the μ-e Electrons

The acceptance of the μ-e electrons ($A_{\mu-e}$) is mutually correlated with the energy spread of the outgoing electron by the energy loss in the target and the momentum acceptance of the secondary beam line as well as the momentum cut required to suppress DIO background. Since the sensitivity goal of this experiment is 10^{-14}, the energy threshold to suppress DIO background would be around 102.5 MeV, which is almost 2.5 MeV below the end point energy. This factor will be combined with the transmission efficiency of the beam line, and will be discussed in the following chapters.

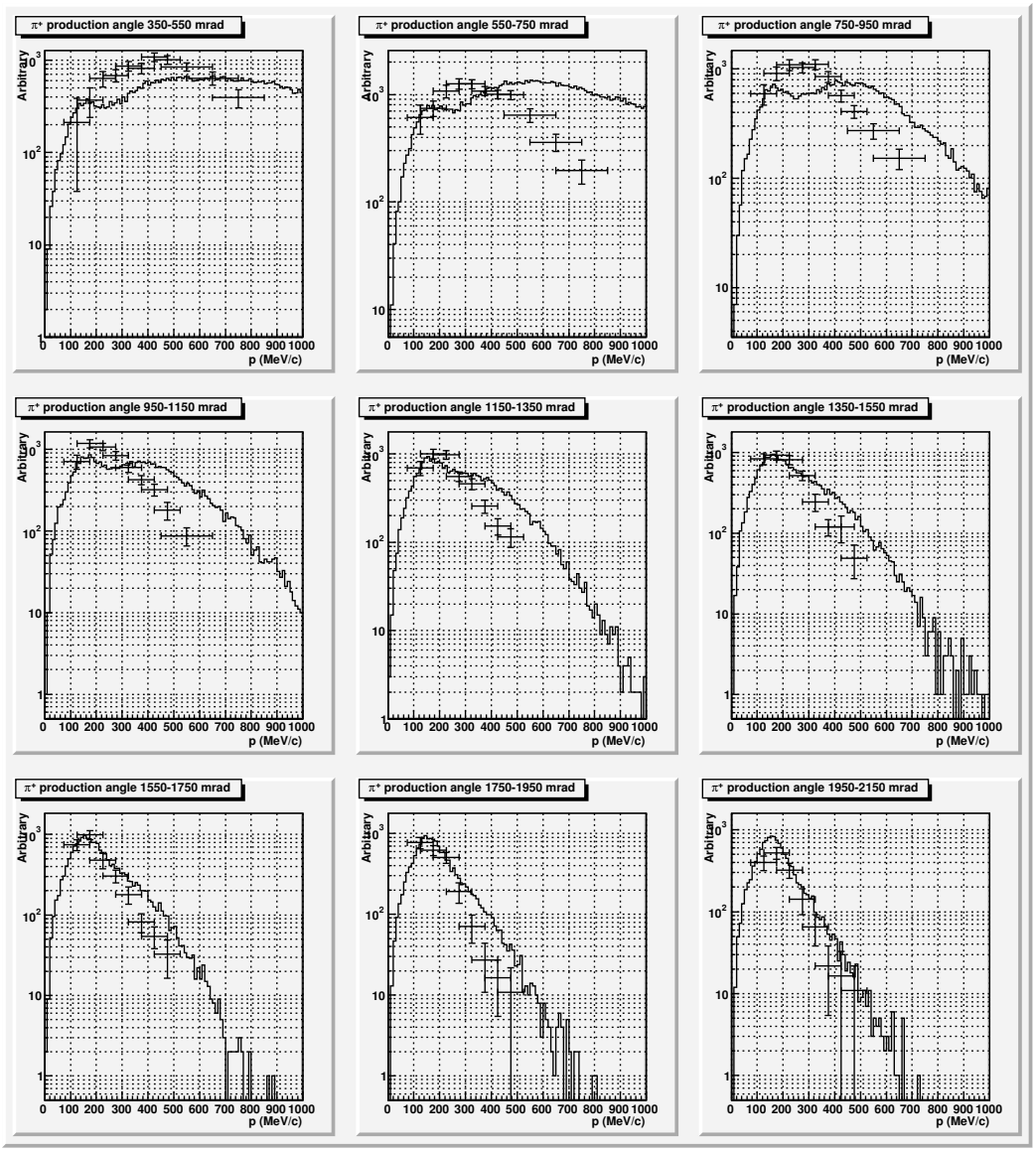

Figure 3.4: Production spectra of π^+ by 3-GeV protons hitting 20-mm thick carbon target, displayed in different angle bins. Histograms are calculation with Geant4 and QGSP_BERT_HP hadron package. Points with error bars are taken from HARP data. Data points are properly scaled so that they give production rate but the cross section itself.

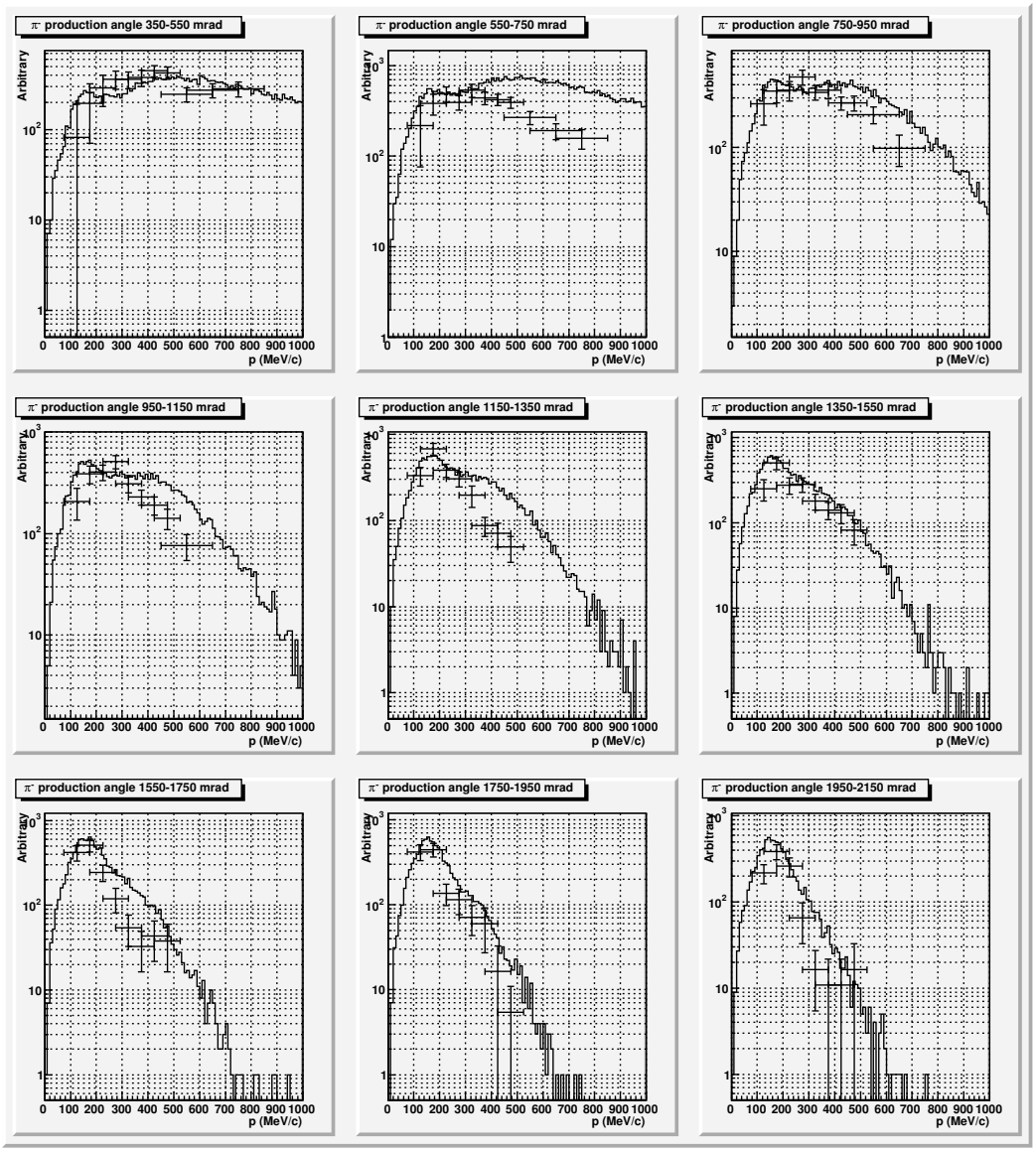

Figure 3.5: Production spectra of π^- by 3-GeV protons hitting 20-mm thick carbon target, displayed in different angle bins. Histograms are calculation with Geant4 and QGSP_BERT_HP hadron package. Points with error bars are taken from HARP data. Data points are properly scaled so that they give production rate but the cross section itself.

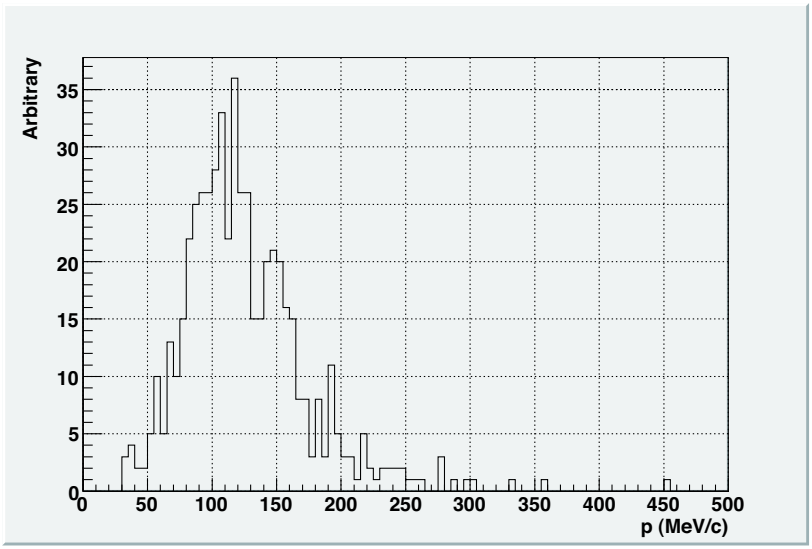

Figure 3.6: Production momentum spectra of π^- by 3-GeV protons hitting 20-mm thick carbon target with a condition requiring the daughter muon coming from its in-flight decay stops in the production target.

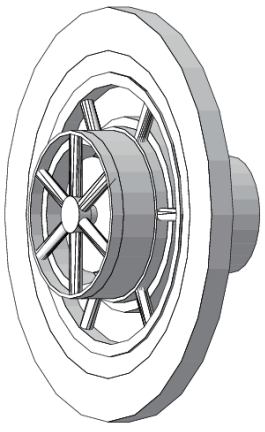

Figure 3.7: A 3D model of the rotation target implemented in Geant4 code.

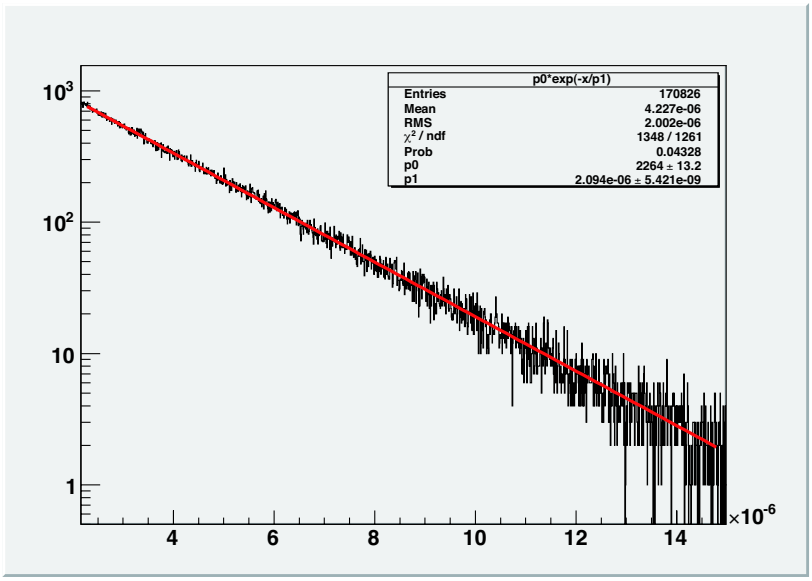

Figure 3.8: Typical time spectrum of delayed-timing charged particles observed at the exit of D-line. The origin of horizontal axis is a time of the 1st proton pulse. In order to protect the counter from the prompt burst, signal at around the proton pulses are masked.

Chapter 4

Measurement at D-Line

The measurement by using the existing D-line in the Muon Science Facility (MUSE) at J-PARC MLF is described in this chapter. The advantage to use the existing D-line is in the cost and schedule. But, the sensitivity at D-line is not attractive due to smaller acceptance of the beamline than that of H-line. Nonetheless, the measurement at D-line will be discussed here in order to illustrate the whole idea of the proposed experiment.

4.1 D-Line

A D-line is the beamline constructed at first in the Muon Science Facility[43]. Figure 4.1 shows the layout of the beamline. The beamline extracts charged particles from the Muon Production Target with 60° angle from the primary proton beam axis. In order to avoid the magnetic-field leakage from the beamline affecting the primary proton orbit, the first quadrupole, DQ1, has to be placed almost 60 cm away from the beam spot on the Muon Production Target. The charged particles are firstly collected by a DQ1-DQ2-DQ3 triplet, and momentum analyzed by a 1st dipole magnet DB1. Then, the beam enters to a superconducting solenoid (DSOL), where the beam is transported in helical trajectory in the DSOL. The original purpose of the DSOL is to increase the muon production from the pion in-flight decay in the solenoid. However, for the μ-e conversion experiment (as well as surface muon experiments), the solenoid is just used for the charged particle transportation. In the solenoid, electrons in the helical trajectories turn around the axis by 3.5 times in transverse plane before emerging out of the solenoid. All the beamline component down to the DSOL are installed in the tunnel surrounded by the radiation-shielding concrete cast. After emerging out of the DSOL, the electron beam is focused by a DQ4-DQ5-DQ6 triplet, and is bent by the second dipole DB2. Then it passes through the electro-static mass separator. The original purpose of the mass separator is to separate electrons from muons for the surface-muon application, but both the electric and magnetic field in the separator will be turned off for the μ-e conversion experiment. After passing through the separator, the beam is focused again by a DQ7-DQ8-DQ9 triplet and enters to a switch yard section. The switch yard section consists of a switch-yard

magnet, a couple of kicker magnets, another switch-yard magnet and a septum magnet (DSEPTUM), in this order from upstream. The DSEPTUM has two entries in front: the beam enters left-side entry is bent towards Area-D2, and the beam enters right-side entry is bent towards Area-D1. The bend angle by the DSEPTUM is 36° for both paths. Two switch-yard magnets are adjusted so that the electron beam enters the left-side of DSEPTUM entrance when the kickers are off. The beam is kicked toward Area-D1 when the kickers are on.

The magnetic field of the kickers is optimized for 30-MeV/c surface muon beam, and is 400 Gauss. The surface-muon beam can be bent perfectly into the septum entrance towards Area-D1 by this kickers. However, it is not perfect for the 105-MeV/c electrons. Most of them hit the iron pillar between the two entrances of the septum magnet due to insufficient kick angle.

In the μ-e conversion experiment, delayed electron beam should perfectly pass through the DSEPTUM towards Area-D2, and the prompt-burst beam should be blocked out of the Area-D2. It is not required to transport the prompt-burst beam towards the Area-D1. Therefore, even if the prompt-burst beam hits the magnet pillar , it is OK as long as they do not enter the Area-D2. According to the Monte Carlo calculation, the suppression efficiency (the ratio of the beam rate in Area-D2 between kicker-off and kicker-on) is about 1/1000, which is sufficient enough for our purpose. The detail of the suppression factor will be described in the following sections.

The beam after the DSEPTUM will be focused again by a DQ13-DQ14-DQ15 triplet toward the experimental area Area-D2, where a magnetic spectrometer will be placed.

4.2 Magnetic Spectrometer

Figure 4.2 shows the schematic layout of the spectrometer system in the Area-D2. The magnetic spectrometer consists of a simple dipole (DB4) sandwiched by two sets of tracking stations (WC1–2 and WC3–4). Each tracking station measured the hit position in 2D coordinate (horizontal and vertical). The horizontal resolution should be better than 400 μm, but the vertical resolution could be much worse. There is a trigger hodoscope (BH1) and the time-of-flight (TOF) hodoscope (BH2) located downstream of the spectrometer.

The distance between BH1 and BH2 is limited by the available space in the Area-D2, and is about 1.8 m in the current layout. The main purpose of the TOF is two folds:

1. identify forward-going electrons from forward-going muons at 105 MeV/c,

2. identify backward-going charge particles.

For examples, it will be used to reject backgrounds coming from cosmic-ray muons hitting through the spectrometer. The minimum performance required for the TOF is to separate forward-going electrons from muons, and it is 1.7 ns for 1.8 m of flight length. It is very easy to achieve this specification by using a standard counter

Table 4.1: Enge coefficients of the quadrupole magnets.

Magnet	a_1	a_2	a_3	a_4	a_5	a_6
DQ1	0.8609	4.694	-2.580	2.592	-1.767	0.4782
DQ2	0.5873	5.894	-0.5713	5.784	2.947	-1.054
DQ3	0.7430	4.791	-2.468	2.407	-1.815	0.6668
DQ4	0.9244	4.848	-2.527	2.328	0.222	-0.4(-0.5564)*
DQ5	0.6109	5.808	-1.037	4.939	2.315	5.946
DQ6	0.6587	5.483	-1.656	3.598	-1.514	0.1493
DQ7	0.9485	4.796	-2.603	1.892	-0.1195	-0.1(-0.2273)*
DQ8	0.6581	4.918	-2.345	2.400	0.3797	-0.08942
DQ9	0.7085	5.193	-2.361	2.296	-1.436	0.9199
DQ13	0.7078	5.249	-2.457	2.027	-0.8117	0.5792
DQ14	0.6607	4.911	-2.318	2.479	0.2345	-0.4319
DQ15	0.7085	5.194	-2.361	2.295	-1.437	0.9220

* The coefficients in parentheses are the one obtained from the field measurement, but not used in the G4Beamline calculation in order to avoid a bug of G4Beamline code.

technique in the high-energy physics experiment. The details of the spectrometer system will be described in the chapter 6.

4.3 Beamline Acceptance

The geometrical acceptance of the D-line was estimated by using G4Beamline. Figure 4.3 shows the model that was implemented in the G4Beamline for this study. The fringing field of all the quadruple magnets are properly modeled in the G4Beamline as a form of Enge parameters. The Enge parameters were obtained from the field measurement. Table 4.1 shows all the Enge parameters used in this calculations. The fringe field of the dipoles are modeled by using an ideal fringe field for the square magnet[45]. Table 4.2 shows the settings of the magnets in the G4Beamline. These settings are based on the real settings obtained from the beam tuning, but the fine tuning in the G4Beamline simulation was applied in order to absorb the small differences between the real world and the computer model. The electro-magnetic separator will be not used in the μ-e conversion experiment, thus is omitted from the table.

Figure 4.4(a) shows electron spectrum produced with uniform momentum distribution in the symmetric direction at the origin of D-line (center of the target position). The vertical axis is normalized so that it gives the transmission efficiency per MeV/c. From this plot, the geometrical acceptance of this beamline is estimated to be 30 msr at 105 MeV/c if it is from the point source. This value is consistent with the observed acceptance of the surface muon, where the source is point like. Drop of the efficiency

Table 4.2: Specification of D-line magnets in the simulation.

Quadrupoles			
Magnet	Field Gradient (T/m)	Length (m)	Pole-Tip Radius (mm)
DQ1	3.004	0.324	125
DQ2	-2.381	0.506	150
DQ3	1.700	0.400	150
DQ4	-2.487	0.413	100
DQ5	3.260	0.386	150
DQ6	-2.295	0.398	150
DQ7	0.7615	0.415	250
DQ8	-1.262	0.540	250
DQ9	1.418	0.405	250
DQ13	1.352	0.431	150
DQ14	-1.813	0.540	150
DQ15	1.519	0.405	150

Dipoles				
Magnet	Field (T)	Length (m)	Gap (mm)	Bend (degrees)
DB1 (sector)	-0.3303	—	200	30
DB2 (rectangular)	-0.3989	0.2	200	40
Switch-yard (rectangular)	0.0682	0.180	198	4
DSEPTUM (sector)	0.2212	—	200	36

Kicker			
Magnet	Field (T)	Length (m)	Gap (mm)
Kicker	0.04	0.4	198

in the momentum region 106–110 MeV/c is observed after DSEPTUM. The cause of this drop is due to the rather smaller horizontal width of the DSEPTUM magnet pole. Figure 4.4(b) shows the same plot but the electron sources are distributed in rectangular region (H:30 mm, V:60 mm) around the origin of D-line, which reflect the source distribution for μ-e conversion electrons. The transmission efficiency drops in two locations along the beamline, one is at the SC entrance, and the other is at the DSEPTUM entrance. The averaged beamline acceptance for μ-e conversion electrons is only 11 msr for this case. The momentum bite is 5 MeV/c(FWHM) for both point-like and distributed source.

The wide momentum acceptance is preferable so that the following three momentum regions can be covered at the same time:

1. DIO region (100–102.5 MeV/c),

2. signal region (102.5–105.0 MeV/c),

Table 4.3: Specification of the kicker system in D-line.

Magnetic Field	400 Gauss
Gap	198 mm
Width	318 mm
Length	400 mm
Rise Time	< 300 ns
Flat Top	> 300 ns
Flatness	$< \pm 3\%$
Repetition	25Hz
Maximum Current	6.3 kA
Peak Voltage	42 kV

3. high-momentum background region (> 105.0 MeV/c).

The last one is important to monitor the background coming from late-arriving protons. In the present D-line, the transmission efficiency of the high-momentum background region is almost 1/3 of the peak transmission at 105 MeV/c, but the efficiency plateau extends up to 115 MeV/c. The integrated efficiency of the high-momentum background region becomes almost the same to that of the signal region. This is very good for the background monitoring.

If the DSEPTUM is replaced with much wider magnet, only necessary to be wide in the left-side horizontal aperture, the overall D-line acceptance for μ-e electrons will be improved by almost factor 2.

4.4 Kicker Performance

The performance of the original kicker that will be installed in the D-line is shown in Table 4.3. The surface muon coming from the upstream of the beamline has a double-pulse structure as shown in Fig. 4.5. In the material science application with the surface muon μSR technique, this double-pulse structure gives no gain to the experimental sensitivity but just disturbs the μSR time spectrum. In order to solve this problem and increase the efficiency of the facility usage, a kicker system is installed to kick the second pulse of the surface muon beam into the second experimental area. Both experimental areas receive a single pulse. The simulated time structure of the current feeding into the kicker is shown in Fig. 4.6. The length of the flat top is about 500 ns, and it is long enough to kick a single pulse.

In the μ-e conversion experiment, the way to use the kicker system is different from the original. Table 4.4 shows the comparison between the two applications. There are three parameters need to be evaluated if the current kicker system should be used for the DeeMe experiment: magnetic field at the flat top period, flatness after the fall edge and the length of the flat top period.

Table 4.4: Comparison between the kicker usage in DeeMe application and the surface muon application.

	Surface Muon	DeeMe
Magnetic Field	400 Gauss	$>$ 400 Gauss
Flatness on the Flat Top	$< \pm 3\%$	—
Rise Time	$<$ 300 ns	—
Fall Time	—	$<$ 300 ns
Flat Top	$>$ 300 ns	$>$ 900 ns*
Flatness after Fall Edge	—	$< 5\%$
Repetition	25Hz	25Hz

* in DeeMe application, the definition of "Flat Top" is the period with the magnetic field larger than the required value. It is not necessary to be "flat".

4.4.1 Magnetic Field of Kicker

The electron beam momentum in the DeeMe is 105 MeV/c, which is 3.5 times larger than the surface-muon beam momentum (30 MeV/c). If we have to completely switch the beam trajectory between two entrances of the DSEPTUM for the 105-MeV/c electrons, we have to increase the magnetic field by factor 3.5, and that is not trivial since the stored energy of the magnet becomes almost one orders of magnitudes higher. However, in the DeeMe application, the function of the kicker system is only to reject the prompt-timing electrons out of the beamline towards Area-D2. Therefore, the kick angle required can be much lower than the surface-muon application. The required performance of the kicker should be optimized by looking at the suppression factor on the prompt burst beam.

In order to estimate the suppression factor on the prompt with the current kicker specification, a Monte Carlo simulation by using G4Beamline was performed. Figure 4.7 shows how the 105-MeV/c electrons are transported through the kicker system towards the Area-D2 while the power to the kicker is off. Figure 4.8 shows the beam trajectories when the kicker is turned on to the designed magnetic field (400 Gauss). As it can be observed from these plots, the electron beam is deflected to the right-hand side while the kicker is on, but not perfectly enters to the beamline towards the Area-D1. However, none of the track passes through the DSEPTUM to the Area-D2 in this plot. This demonstrates that the current kicker system can cut off the beam with large suppression factor. By increasing the simulated statistics, it was found that the suppression factor of the electron beam passing through the left-side aperture of DSEPTUM and entering to the Area-D2 is about 1/1200. It will give the rate of the prompt-burst particles entering to the Area-D2 at around 33k per proton pulse. The both plastic scintillation counters and gas wire chambers can be operated under this condition if they are properly segmented. The details of the detector technology will be discussed in Chapter 6.

4.4.2 Flatness after the Fall Edge

It is note worth that there is no requirement to the flatness of the "flat top" for DeeMe application. DeeMe only needs the beam kicked out of the beamline, and it does not care where the kicked beam is going. The magnetic field during the "flat top" should be larger than the required field strength in order to maintain the suppression factor.

While the flatness of the flat-top is not required, the flatness after the fall edge is important for the proposed experiment since μ-e electrons in the delayed timing has to be transported through the beamline after the fall edge. The horizontal displacement of the beam center by the kicker is about 100 mm for 400 Gauss, thus it is only 5 mm for 20 Gauss. Since the horizontal beam size at the DSEPTUM entrance is about 100 mm(FWHM), The effect of the 5 mm displacement is small enough. Therefore, if the flatness of the kicker after the fall edge is less than 20 Gauss, then it is acceptable. From the Fig. 4.6, the non-flat structure after the fall edge is only $< 5\%$, and it is small enough.

4.4.3 Flat Top Length of the Kicker

In the DeeMe application, both of two pulses separated by 600 ns should be kicked out of the beamline. Therefore, the flat top has to be wide enough to cover the pulse separation (600 ns) with enough margin to cover the pulse width (200 ns), and it should be more than 800 ns in total. The fall time of the kicker should be fast enough so that the detector can start the measurement of the delayed electrons as soon as possible. On the other hand, there is no requirement to the rise time itself.

The pulse current for the present kicker is shaped by a pulse forming network (PFN) made of discrete capacitor and inductor components. Figure 4.9 shows the schematic circuit diagram of the kicker power supply. Rise and fall time of the kicker system are determined by the cut off of the circuit in the frequency domain, and that is dominated by the inductance of the magnet. Changing the rise and fall time may need complete redesign of the kicker magnet, but very fortunately, the kicker parameters of the present system ($T_{\rm rise} < 300$ ns, $T_{\rm fall} < 300$ ns) are sufficient for us.

The flat top length is determined by the number of stages in the PFN circuit. It is fairly straight forward to increase the flat top: just increase the number of stages. The number of stages is 15 in the current system for 500 ns of the flat top length. It has to be increased to 30 to make the flat top length > 800 ns. It may be also possible to use the different parameters of both capacitor and inductor in each stage so that the flat top length becomes > 800 ns with smaller number of stages. In that case, the flatness of the flat-top will be deteriorated, but as it was explained above, it is fine for μ-e conversion experiment as long as the magnetic field is larger than 400 Gauss.

The modification of the circuit has to be done so that the switch back to the μSR program is easy and quick. The best way might be constructing a new PFN module for μ-e conversion, and connect it to the existing circuit with a changeover switch.

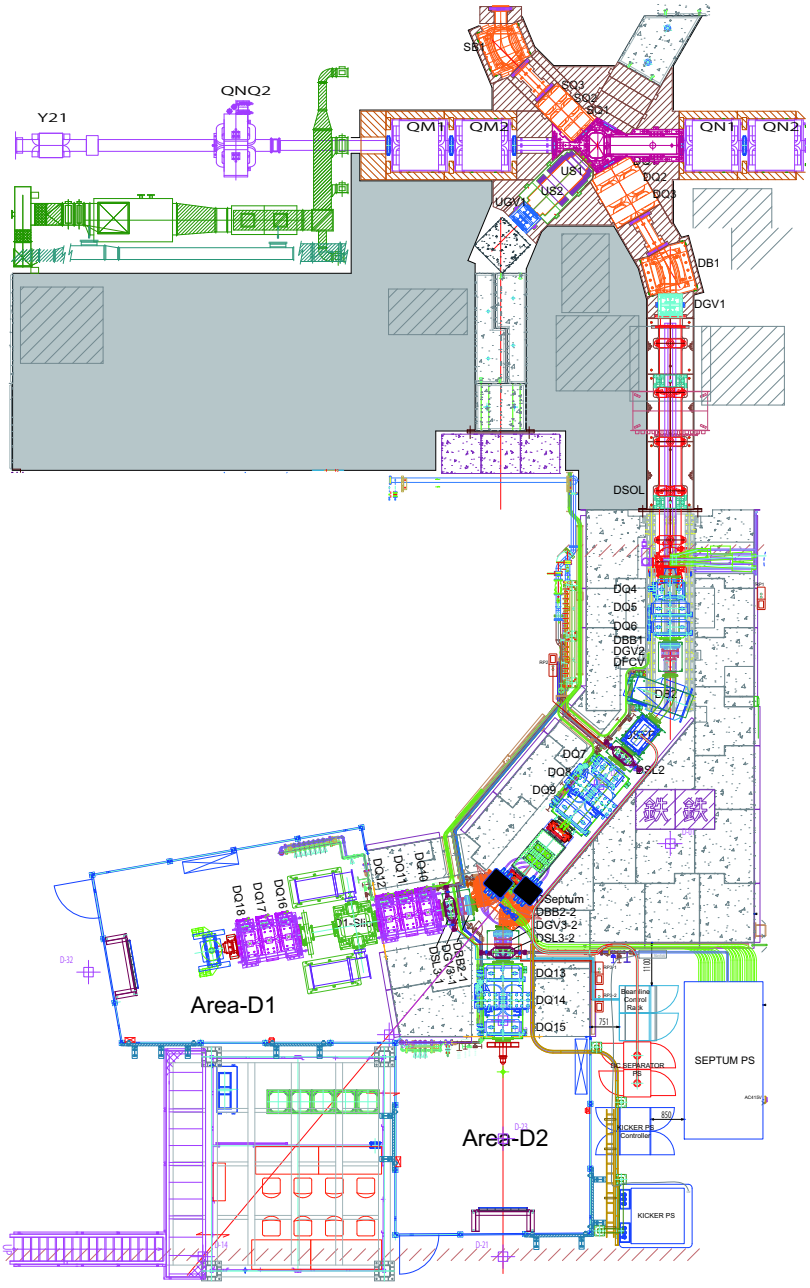

Figure 4.1: Layout of the D-line in the Muon Science Facility at J-PARC MLF.

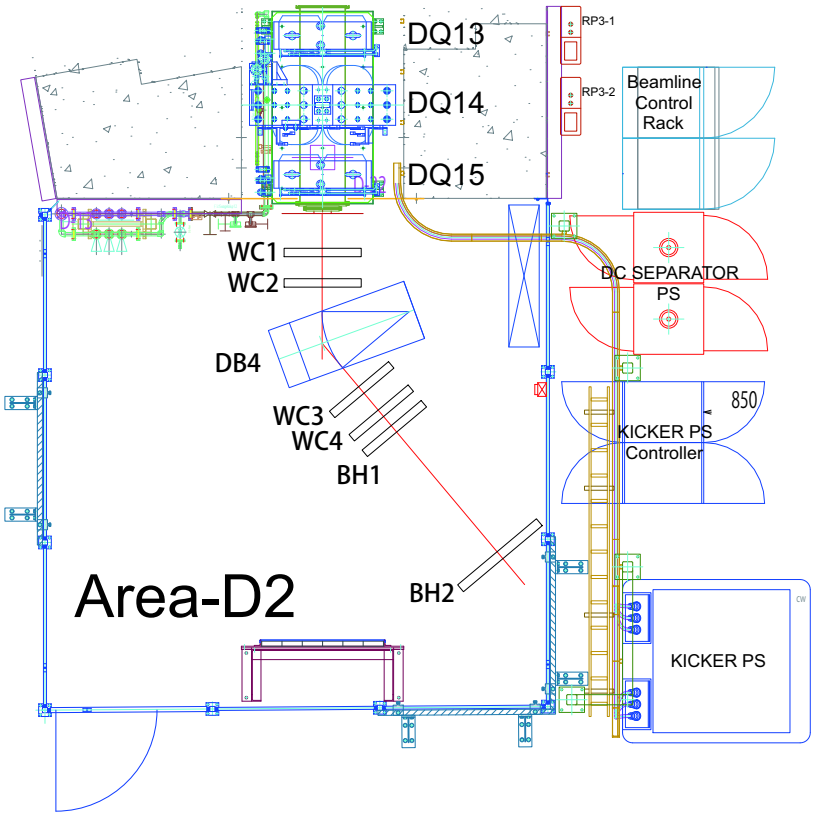

Figure 4.2: Schematic layout of the magnetic spectrometer system in Area-D2.

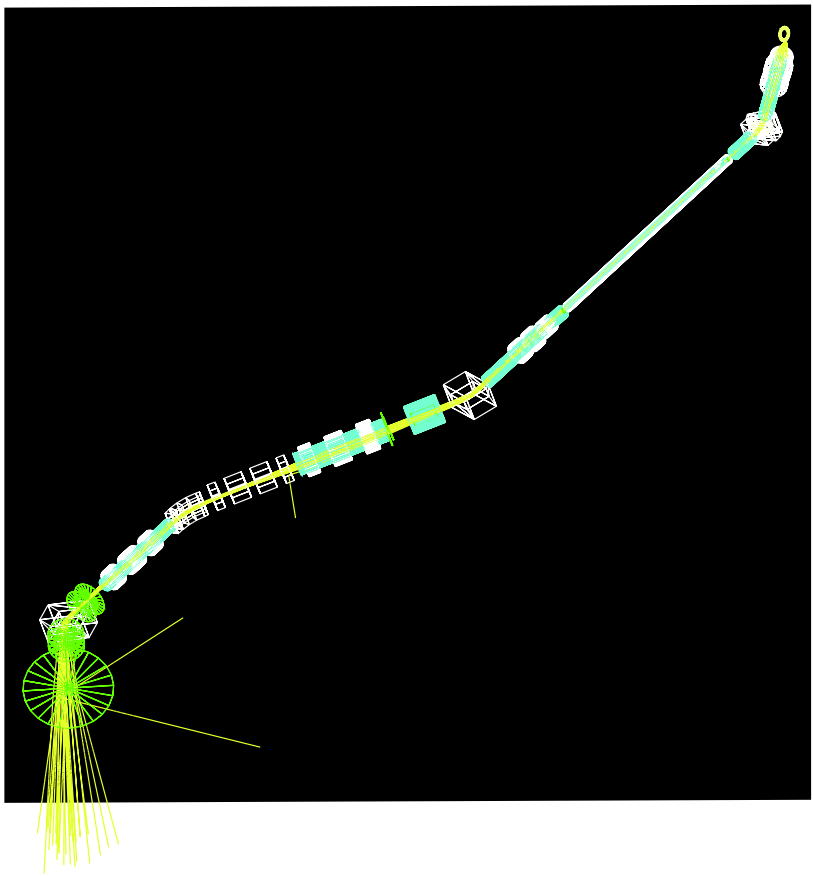

Figure 4.3: A model of the D-line that was implemented in the G4Beamline simulation code for the beamline acceptance evaluation.

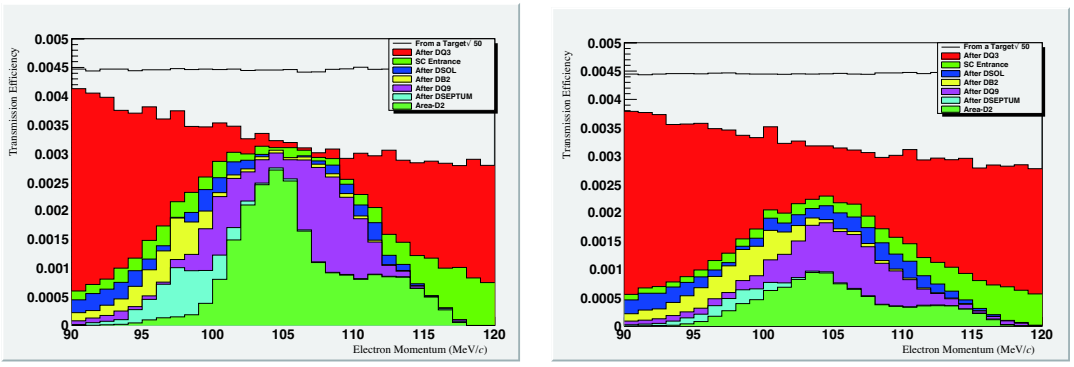

(a) Point source at the origin of D-line. (b) Distributed source (H:30 mm×V:60 mm)

Figure 4.4: Electron transmission efficiencies of the D-line, displayed with several different places along the beamline.

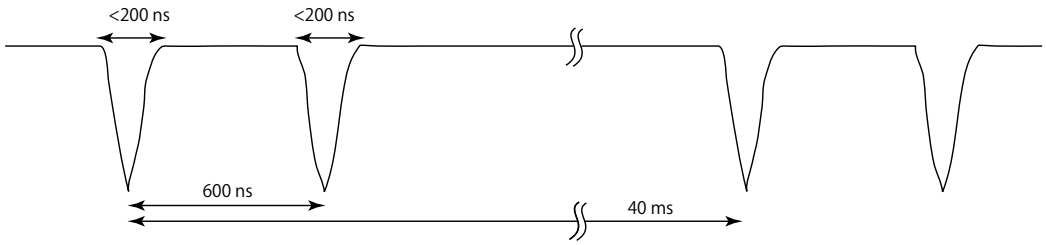

Figure 4.5: Time structure of the pulsed proton beam from RCS to MLF.

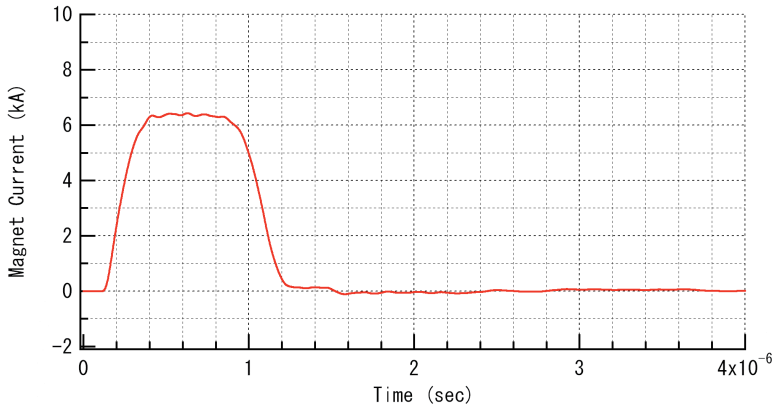

Figure 4.6: Simulated time structure of the current from the power supply to the kicker magnet.

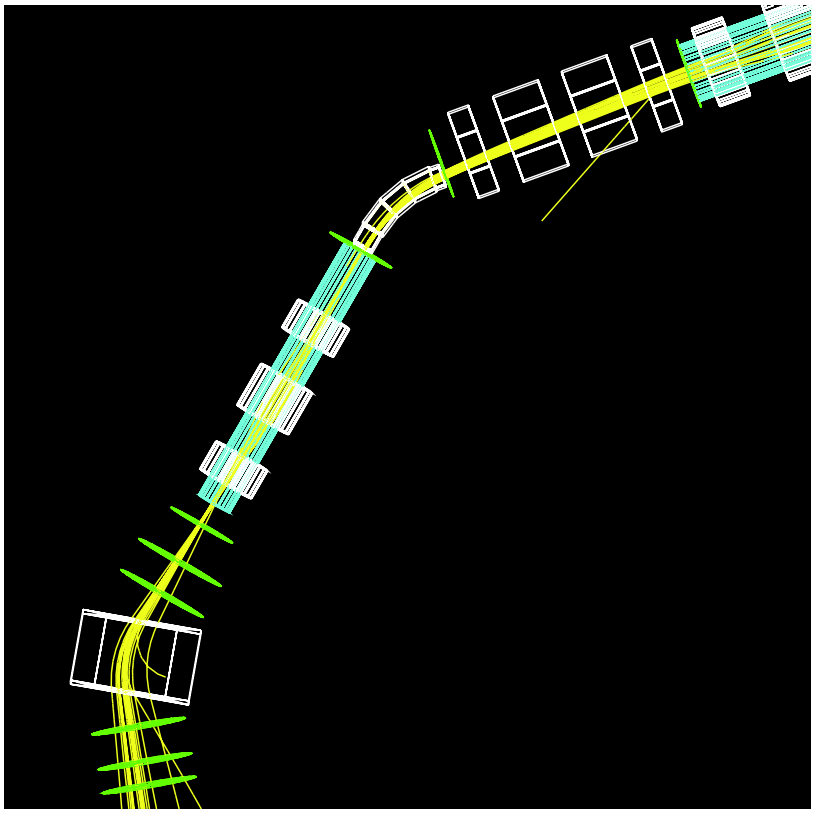

Figure 4.7: G4Beamline display showing the trajectories of 105 MeV/c electrons during kicker is off.

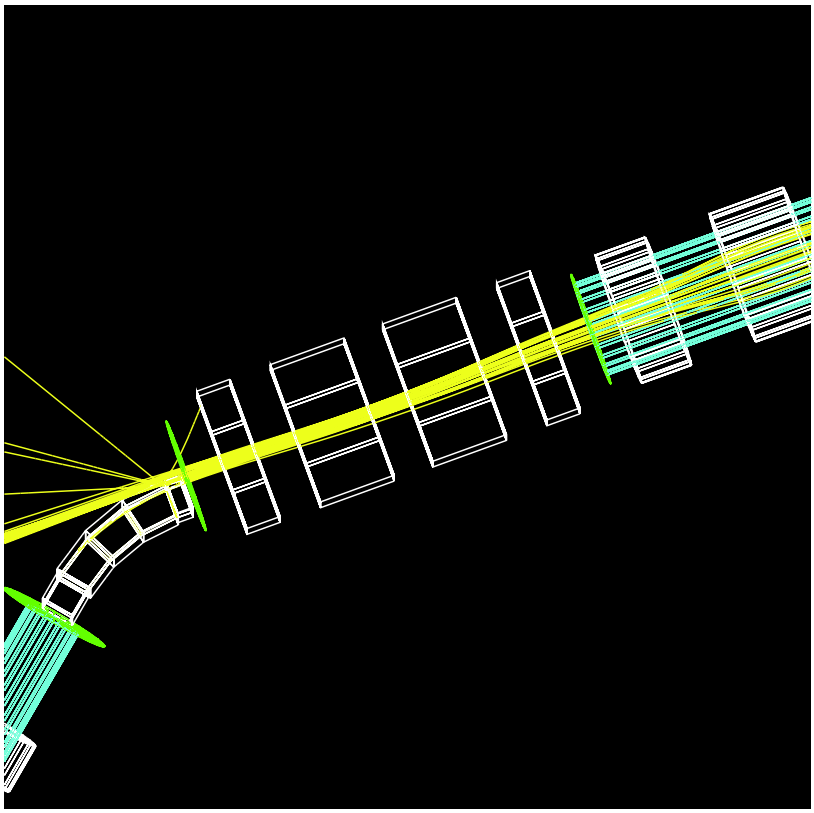

Figure 4.8: G4Beamline display showing the trajectories of 105 MeV/c electrons during kicker is on. Note that the right-hand side of the DSEPTUM is not modeled in the simulation.

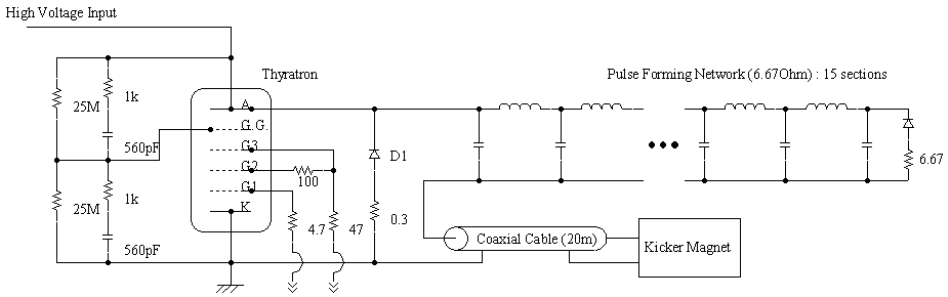

Figure 4.9: Schematic circuit diagram of the power supply with a pulse forming network for the present kicker system at the D-line.

Chapter 5

Measurement at H-line

The experimental sensitivity from the data taking at Area-D2 is limited by the acceptance of D-line. It could be also limited by the conflict with other experiments planning to use Area-D2. Therefore, it is very important to consider running the experiment at a new beamline with larger acceptance, H-line. The geometrical acceptance of H port is almost four times larger than that of D-Line. In addition, the H-line design can be accomplished so that the acceptance averaged over the finite size of the source (H:30 mm $\times$ V:60 mm) being almost the same to that of the point-like source. There is almost factor 3 of the improvement over D-line from this. The overall improvement by moving the experiment from D-line to H-line is one order of magnitude.

Since there are other experiments considering to use the H-Line, muon $g-2$ for example[46], the current design of H-line adopts an idea of hosting multiple experiments by preparing beamline branches.

5.1 Requirement

Table 5.1 shows specifications of the new beamline for three different experiments. They seem to be very different at a glance, but the important specification is the same: maximizing the acceptance. Difficulties of the design for DeeMe come from the requirement asking large acceptance for large source size with large $\Delta p/p$ for high momentum. The first three points require the size of magnets being large, and the last point demands the high magnetic field for those large-sized magnets.

Figure 5.1 shows the original floor plan of the H-line: the High-Momentum Decay Muon with large pion decay solenoid. The requirements shown above are basically compatible with the High-Momentum Decay Muon beamline, which needs large acceptance and large $\Delta p/p$ especially for the upstream side of the beamline if one really need to increase the muon yield. Therefore, the design of the H-line for DeeMe is actually one variation of the original plan.

Table 5.1: Specifications of H-line from three different experiments.

Item	DeeMe	$(g-2)_\mu$	surface muon
Particle	e^-	μ^+	μ^+
p (MeV/c)	105	30	30
$\Delta p/p$(FWHM)	10%	10%	10%
Source Size (H)	30 mm	15 mm	15 mm
Source Size (V)	60 mm	30 mm	30 mm
Acceptance (msr)	120	120	120
Final Focus Size	any	smaller is better	
Electro-static Separator	—	e^+ suppress	
Kicker	prompt suppress	—	—

5.2 Optics Design

Figure 5.2 shows the new design of H-line that we propose. The main beamline is for μ-e conversion experiment, and there are two branches from the main beamline for $(g-2)_\mu$ and a surface-muon experiment. The beam takes off from the production target at an angle of 60 degrees to the proton beam direction. There is a flange with 25 cm diameter inner aperture at 51 to 60 cm from the production target. This restricts the accepted solid angle to 135 msr, averaged over the source size. Since some beam loss in the beam line is unavoidable, the final acceptance is of the order of 115 msr for the central momentum.

Solenoid S1 catches a large solid angle, and focuses the beam through the 30 degrees bending magnet B1. It was necessary to find a place for a separator that can remove positron from the surface muon beams. The prompt suppression for the DeeMe beam has to be high enough. But it was also necessary to maintain a high solid angle acceptance. All those aims are accomplished with the layout already shown in the Fig. 5.2. Solenoid is followed by two kickers, K1 and K2, and the separator. Then comes solenoid S3 and the other two kickers, K3 and K4. To obtain good beam transmission for the DeeMe beam, a small n-value of -0.40 had to be put in B1 for additional horizontal focusing. This feature could be eliminated in future designs. Bending magnet B2 is off for DeeMe. It bends 45 degrees to the left followed by a quadrupole doublet Qdoub for surface muon experiments. The final beam spot is 1.00 m downstream of the exit of Qdoub.

When B2 is turned off, the beam continues to the DeeMe line. First, there are again two solenoids, S4 and S5, which focus the beam through the 435 degrees bend B3 to make the beam size smaller downstream of B3 at the point indicated by INT. B3 bends 45 degrees to the left. The rest of the beam line consists of a quadrupole triplet Qtrip and a 45 degree bend B4. This part is very important to increase the suppression factor against the prompt burst since the electrons scattered off by slits will not enter B4 due to the energy loss. It can also act like a spectrometer if necessary. The first and last quadrupole of Qtrip have the same field. Beamline monitor can be

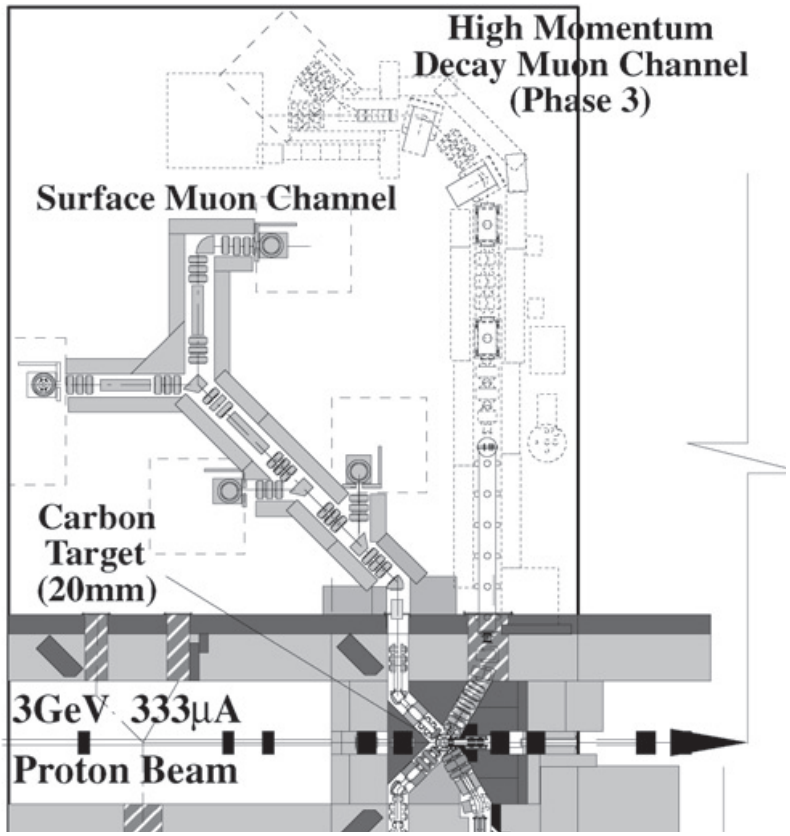

Figure 5.1: Originally proposed layout of the H-line, High Momentum Decay Muon Channel.

placed at the point indicated by INT, right after B3, for beam tuning and monitoring. The magnetic spectrometer system will be installed at downstream of B4.

Solenoids rotate the beam around the beam axis, mixing horizontal and vertical phase space. It is not an issue for S1. However, there is momentum dispersion after B1, and solenoids cause then also dispersion in the vertical plane. This is undesirable because it is not convenient for the measurement of the momentum with the final spectrometer. Therefore, the polarities of S2 to S5 are alternating, so that the rotation introduced by one solenoid is partly canceled by the next one. The strengths of the solenoids S2 to S5 have been chosen so that the sum of the products of B and L (field strength times length) is zero. Then the rotation of the beam caused by the combined effects of S2 to S5 is zero. Therefore, there is no dispersion in the vertical plane.

For the surface muon beam, S2 and S3 will be adjusted to have equal but opposite strength. In that case there is no vertical dispersion after S3. There is a slit, named SLIT, 30 cm downstream of kicker K4 for surface muon beams. When the B2 is turned off, the beam continues with a triplet to a final focus for the muon $g-2$ experiment.

Table 5.2: Characteristics of solenoids at 105 MeV/c for μ-e conversion mode.

Solenoid	Length (m)	radius (cm)	Field (kG)
S1	1.50	30.0	5.775
S2	1.50	20.0	4.095
S3	1.50	20.0	-2.940
S4	1.50	20.0	-3.360
S5	1.50	20.0	2.205

Table 5.3: Characteristics of quadrupoles of Qtrip for μ-e conversion mode.

Quad	Length (m)	radius (cm)	Field (kG)
Qtrip-1	0.4	17.5	-1.5354
Qtrip-2	0.4	17.5	2.5045
Qtrip-3	0.4	17.5	-1.5354

5.2.1 Magnets

The characteristics of the solenoids have been listed in Table 5.2. All solenoids are 1.5 m long with a 40 cm diameter, except S1 which has a 60 cm diameter. It was designed so explicitly in order to reduce the mass production cost of the solenoid. The characteristics of the quadrupoles are given in Table 5.3. All quadrupoles are 40 cm long with a 35 cm diameter. The characteristics of the bending magnets are given in Table 5.4. Bending magnets B2, B3 and B4 are 45 degrees sector magnets. B1 is a parallel faced magnet which bends 30 degrees. It has an n-value to provide horizontal focusing.

The kickers are each 40 cm long with a horizontal aperture of 35 cm and a vertical aperture of 32 cm. Each kicker kicks the 105-MeV/c electrons horizontally by 32.0 mr, and a total kick is 128 mr. This implies a vertical magnetic field of 280 Gauss for 105 MeV/c. In this case the transmission from the production target to the point INT is less than 0.010 percent.

Table 5.4: Characteristics of bends at 105 MeV/c for μ-e conversion mode.

Bend	Bend (degrees)	Pole-face Rotation (degrees)	Field (kG)	n-value
B1(rectangular type)	30	15/15	2.2923	-0.40
B2(sector type)	60	0/0	0.0	—
B3(sector type)	45	0/0	3.4385	—
B4(sector type)	45	0/0	3.4385	—

The separator has a physical length of 1.40 m, but the length of the fields is 0.80 m. An electric gradient of 12 kV/cm is sufficient to reduce the positron contamination in the surface muon beams by a factor 100. The magnetic field is 146 Gauss.

5.2.2 Beamline Simulation

The design calculation have been done with the Monte Carlo program REVMOC[47]. The source of the electrons from the μ-e decay is assumed to be a disk with a diameter of 6 cm based on the present Muon Production Target. By projecting it at right angle to the secondary beam axis, the source becomes an ellipse with axes of 3 cm horizontally by 6 cm vertically. In fact, in the Monte Carlo calculations, a rectangular, uniformly populated source of 3 cm by 6 cm was used. Although the beamline design was performed with assuming the fixed-type target, it is also valid for the rotation target since the source distribution will be about the same around the beam center.

Figure 5.3 shows the final beam spot at the bottom and the solid angle acceptance as function of momentum at the top, for 105-MeV/c electrons. This solid angle acceptance is more than 110 msr for large-area source size, and which it almost one order of magnitude larger than that of D-line. Please note that the acceptance improvement will be only factor 4 if the source distribution is point-like. The momentum bite is $\Delta p/p = 7.0\%$ at the final focus, and the beam size is 11.4 cm(FWHM) horizontal and 13.8 cm(FWHM) vertical. This seems to be large, but it is fine for μ-e conversion experiment since the beam only passes through the magnetic spectrometer.

In the μSR mode, the size of beam spot is 2.8 cm(FWHM) horizontal and 6.8 cm(FWHM) vertical. In the muon $g-2$ mode, the size of beam spot is 2.7 cm(FWHM) horizontal and 5.0 cm(FWHM) vertical.

5.3 Realistic Considerations

There are several things those have to be considered when this optics design is implemented to the available space and conditions in the real world of the muon facility.

Available Space As it is observed in the Fig. 5.1, the available space for H-line is limited between the surface muon channel and neutron facility area. The beam axis of the current design mostly runs parallel to the boundary and the distance between the beam axis and either the surface muon channel or the neutron facility area is more than 4 m, which is wide enough. The distance between the end of B4 and the radiation shield block of the surface muon channel is more than 4 m, which is long enough to install magnetic spectrometer system including a time-of-flight hodoscope.

Gate Valve A gate valve has to be installed in the upstream region of the beamline. Since the largest gate valve currently available from the market has 25 cm inner diameter, the beam size should be smaller than 25 cm diameter preferably before the beamline entering the experimental hall. In the current optics design, the beam size is larger than 25 cm upstream of B1, but it is smaller than 25 cm downstream of

B1. So, the gate valve can be installed anywhere between 1-m downstream of B1 and S2. A thin foil for blocking the radioactive ions produced at the production target transporting into the experimental area can be also placed at the position of the gate valve.

Current Lead for Superconducting Solenoid Although S1 has to be built with radiation-hard MIC wires, all the other solenoids can be superconducting magnet in order to reduce the operation cost. In that case, each solenoid has to have a space for a port, where current leads and coolant pipes are attached. The downstream end of S2 is located just at the exit of the tunnel, and the space between the tunnel exit and the kicker is about 1 m. This space can be used for the port of S2 solenoid.

Cable Rack in the Tunnel There is a cable ruck installed in the tunnel. The position is just above the space for a beam duct, downstream of S1 and the upstream of B1. The installation of a simple beam duct underneath the cable rack is needed, but it is much easier than installing magnets itself underneath.

5.4 Magnetic Spectrometer

The performance of the detector system in DeeMe is limited by the rate of the beam burst in the prompt timing. The suppression factor on the prompt beam burst in the new beamline is about 10^{-4}, which is almost one order of magnitudes better than that of D-line, while the beam acceptance is one order of magnitude higher. Therefore, the rate of the prompt beam burst will be about the same in the both D-line and H-line. As a result, the specification of the magnetic spectrometer in the measurement with the new beamline is almost the same to that can be used in Area-D2. The design of the magnetic spectrometer system can be the same between H-line option and D-line option. The details of the detector design will be described in Chapter 6.

5.5 Kicker System

The beam emittance in H-line is much larger than in D-line. Both the aperture of the kicker magnet and the kick angle has to be larger than the kicker system in the D-line. Therefore, the kicker system has to be completely redesigned. Table 5.5 shows the required specification of the kicker system. The main difference between H-line kicker and D-line kicker is the gap size.

Two different types of the kicker systems were considered. One is a double-strip lumped-type magnet driven by two synchronized resonance circuits, and the other is a transmission-line type magnet driven by a pulse forming network circuit. The latter system will be employed for the proposed experiment, but the both system will be described below in order to illustrate the issues of the kicker system.

Table 5.5: Specification of the Kicker Magnet for the measurement at H-line.

Magnetic Field	> 385 Gauss
Gap	320 mm
Width	320 mm
Length	400 mm
Number of Kickers	4
Fall Time	< 300 ns
Repetition	25Hz

5.5.1 Lumped-Type Kicker Magnet System

Figure 5.4 shows a design model for the TOSCA calculation. A square-type magnet york is made of ferrite material. Two coils are used to magnetize the ferrite, but each coil is a single turn and driven by an independent power supply. The inductance of the coil was estimated to be 2.84 μH for each. The drive current to each coil is 5150 A per 1 T.

In order to fulfill the requirement on the fall time (from 425 Gauss to 0 Gauss within 300 ns) and flat-top length (> 800 ns), each coil is driven by sinusoidal shape current as shown in Fig. 5.5. The frequency is 1.76MHz, and the maximum current per coil is 10 kA. Each coil is connected to the power supply as shown in Fig. 5.6. Since the largeness of the maximum current per coil, the available thyratron would be only e2V CX1836, and the charging voltage is 50 kV. If the two coils are connected sequentially, the coil inductance will be doubled, and the capacitance should be half for the same frequency. Then the charging voltage should be doubled, and that is very difficult. If the coils are connected parallel to a single power supply, the maximum current will be doubled to 20 kA, and there is no available thyratron in the market. Therefore, using double power supplies are essential, and the synchronization of two thyratrons is not trivial.

5.5.2 Transmission-Line Kicker Magnet System

In order to overcome the difficulty of the double-strip lumped-type kicker system shown above, a transmission-line type of the magnet system has been considered. Figure 5.7 shows the sketch of the kicker magnet and its vacuum chamber. A whole magnet consists of multiple ferrite segments, and copper conductors run through the Ferrite cores to form a single turn coil. Ceramic capacitors are connected to the copper conductors in every gap between adjacent Ferrite cores, and make the conductor as impedance-matched signal line. The cutoff frequency of the magnet is dominated by the inductance of single Ferrite. It is not so difficult to make the fall time smaller than 300 ns with the condition of keeping the maximum current less than the double strip design.

Table 5.6 shows magnet parameters for several different sizes of a single Ferrite

core. Figure 5.8 shows a schematic circuit of the power supply. Figure 5.9 shows

Table 5.6: Magnet parameters for the transmission-line kicker system.

Items			
Inductance of Ferrite Core	16 nH	25 nH	31 nH
Impedance	5Ω	5Ω	5Ω
Capacitance	640 pF	1000 pF	1240 pF
Cutoff Frequency	51 MHz	32 MHz	25 MHz
Rise Time	20 ns	32 ns	39 ns
Delay Time per Segment	4.4 ns	7 ns	9 ns
One Segment Length	25 mm	40 mm	50 mm
Number of Segments	64	40	32
Number of Units	$(25\,\mathrm{mm} \times 16) \times 4$	$(40\,\mathrm{mm} \times 10) \times 4$	$(50\,\mathrm{mm} \times 8) \times 4$

a typical waveform for the circuit when the end of the current load is shorted. A glitch due to the reflection by the impedance mismatch exists, but the amplitude is only about 2% whose effect on the electron transmission through the kicker system is negligible. A large current jump at around $2\,\mu$s after the fall edge is due to the reflection and the timing of this jump is determined by the length of the power cable between the magnet and the power supply, which is labeled as T2 in the Fig. 5.8. Since the length of the cable can be much longer, it will never affect the actual measurement of μ-e conversion.

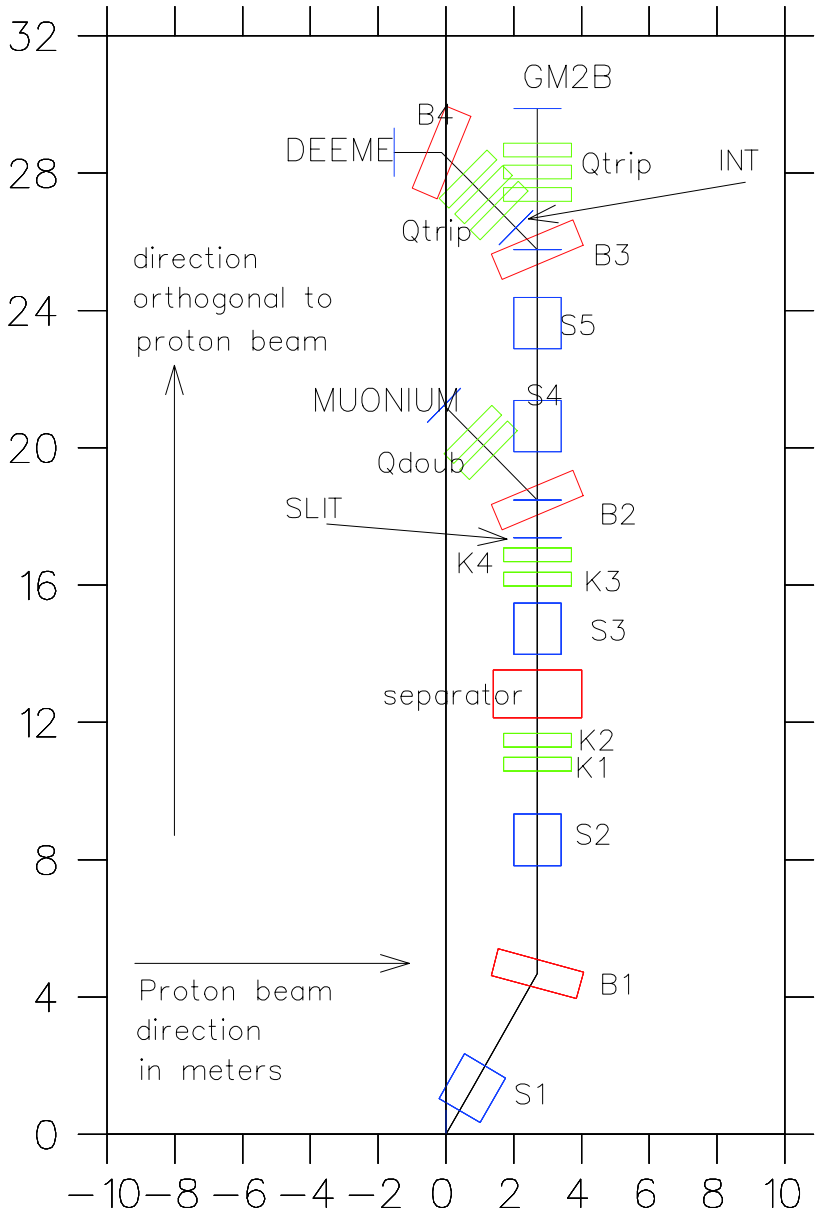

Figure 5.2: Layout of the new beamline for DeeMe (DEEME), surface muon (MUSR) and muon $g-2$ (GM2) experiments. S1–5 are solenoids, B1–4 are dipole bends, K1–4 are kicker magnets, Qdoub and Qtrip are quadruple- doublet and triplet, respectively.

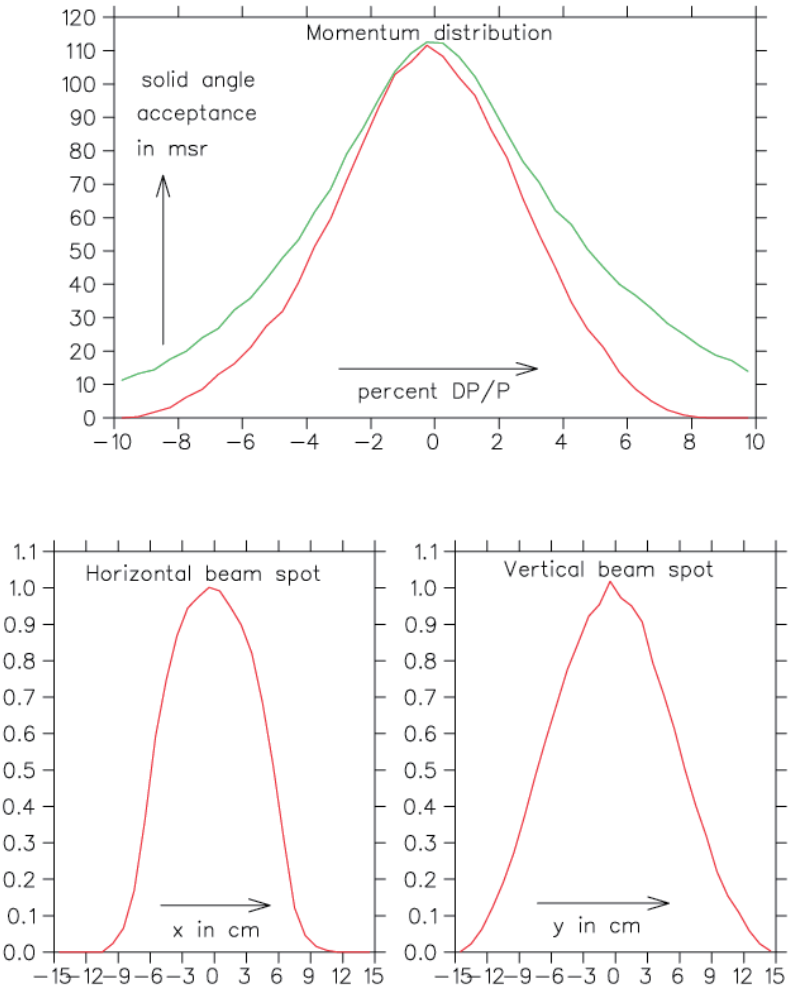

Figure 5.3: Solid angle acceptance as function of momentum. The green curve is for the intermediate point INT. The beam spots are shown in the bottom part.

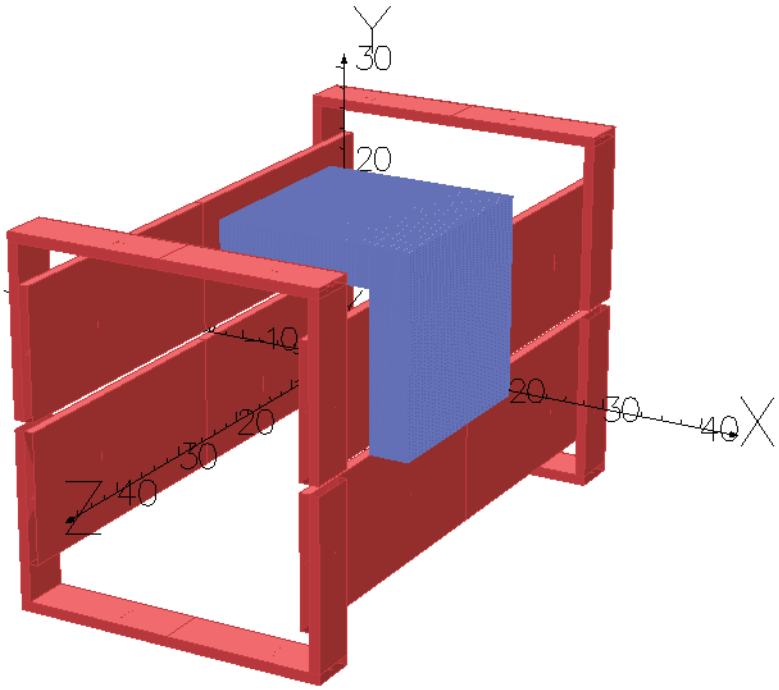

Figure 5.4: A model of a lumped-magnet type kicker. Quota cut of the Ferrite core is shown in a blue-colored volume. Two coils are driven by individual power supplies.

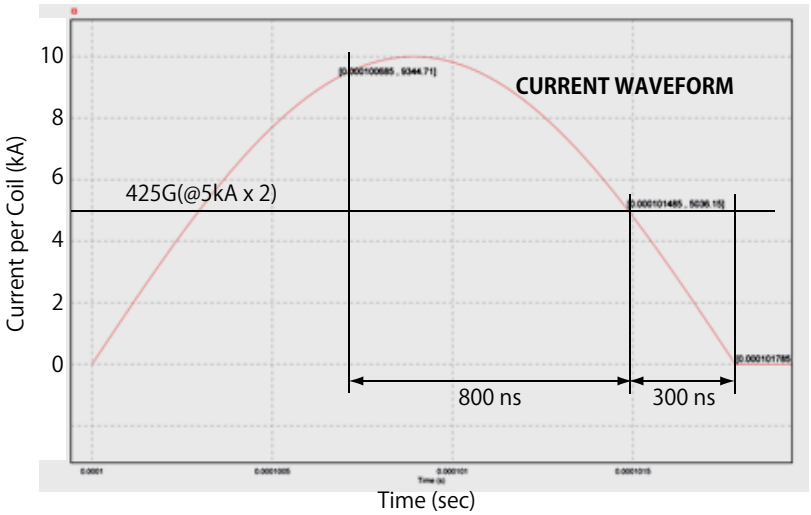

Figure 5.5: The waveform of a current to the lumped-magnet kicker. It is note worth that the flatness of the "flat-top" is not required at all for DeeMe application.

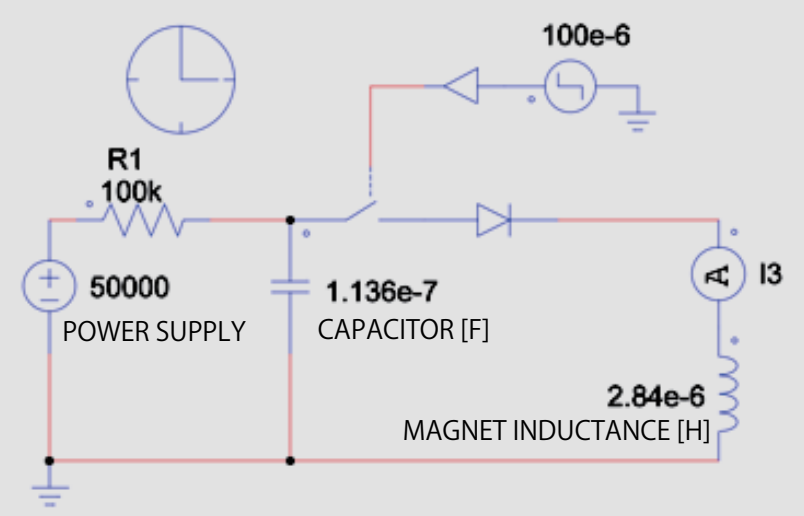

Figure 5.6: Schematic circuit diagram of the power supply for the lumped-magnet type kicker.

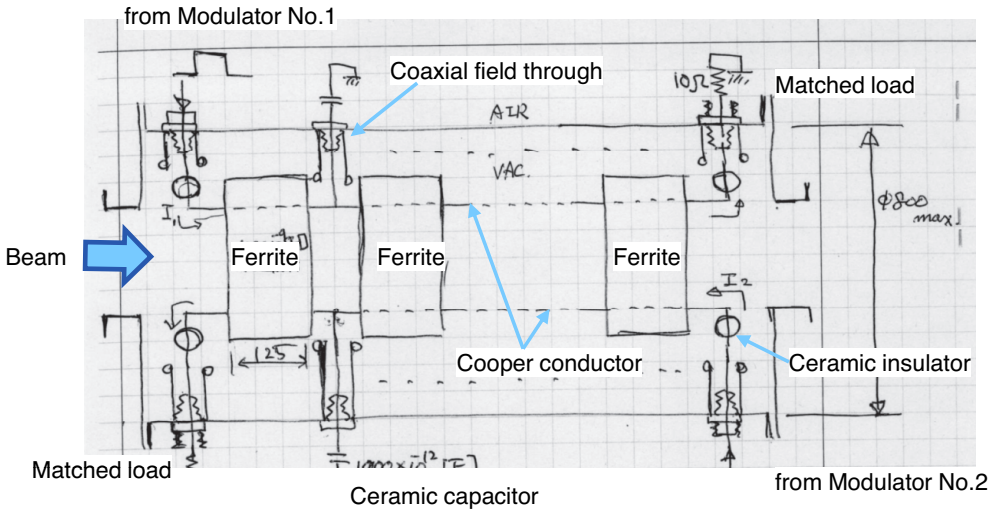

Figure 5.7: Image sketch of kicker magnet and its vacuum chamber.

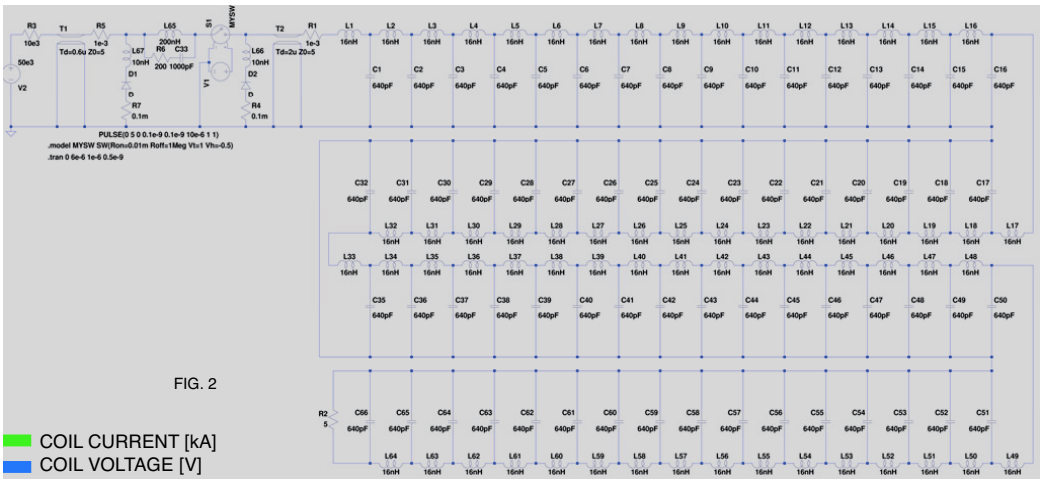

Figure 5.8: Schematic circuit diagram of the transmission-line type kicker system for DeeMe.

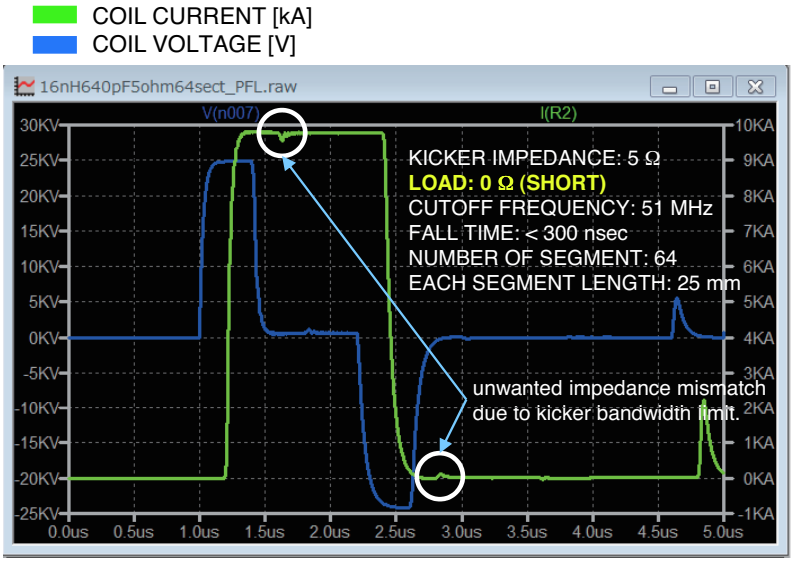

Figure 5.9: Simulated waveform of the transmission-type kicker system. The fall time is less than 300 ns. A bump due to unwanted impedance mismatch due to kicker bandwidth limit is small enough. A jump at around 4.8 μsec is due to a reflection, but can be delayed much more by changing the length of the cable. See the text for more details.

Chapter 6

Detector

Even if the beamline momentum is set at the 105 MeV/c, there will be many particles emerging out of the beam line with other momenta. Most of them are DIO electrons from muons stopped somewhere in middle of the beam line. In order to reject those off-momentum electrons, an electron spectrometer should be installed at the downstream of beam line exit. The electron spectrometer should provide a measurement of the high momentum tail of DIO spectrum simultaneously, which is very important to understanding the DIO background. The momentum resolution should be less than 0.5 MeV/c(rms) in order to separate the μ-e electrons from the DIO electrons.

The detector has to be operational after prompt-burst of the beam. The expected rate of the prompt-burst is about 33k particles per proton pulse. A couple of the prompt-bursts separated by 600 ns will come in every 40 ms. The average rate is less than 2MHz, but the detector design needs some special cares since the beam is not DC beam and the instantaneous rate of the prompt-burst is much over GHz.

The detector system proposed here is a simple magnetic spectrometer with a dipole magnet and several planner tracking chambers. A trigger hodoscope and a time-of-flight hodoscope are needed to define the timing and to reject muon backgrounds. Figure 6.1 shows a schematic layout of the spectrometer system. The required specifications to the detector system are almost the same between the measurement at D-line and the measurement at H-line. Therefore, a generic system that can be used in both cases is discussed here.

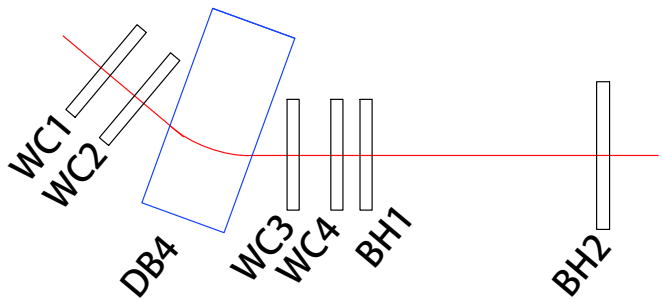

Figure 6.1: Schematic layout of the electron spectrometer

Table 6.1: Required specification of the DeeMe magnetic spectrometer system.

item	parameter
δp	< 0.5 MeV/c
Prompt Burst	33kHz per pulse
No. of pulses	2 per RCS extraction
Repetition	25 RCS-extractions per second
Live Time Window	from 300 ns after the prompt of the second pulse
PID	separation between e^- and μ^- at 105 MeV/c
Charge Separation	separation between e^- and e^+
Directional Separation	separation between forward and backward going e^-

6.1 Detector Requirement

Table 6.1 shows the requirement to the detector system. The most important thing is that the whole detector system should be in operational after a couple of prompt-bursts separated by 600 ns. Each burst would contain 33k charged particles in 200 ns (FWHM). The instantaneous rate is almost 330GHz, but the repetition of the couple of prompt-bursts is only 25 Hz and the average rate is less than 2MHz.

The momentum resolution should be sufficient to distinguish μ-e electrons from DIO electrons. Figure 6.2 shows expected DIO electron spectrum from carbon and aluminum at the energy close to the endpoint energy. DIO electron spectrum from silicon is very similar to that of aluminum, so the aluminum spectra are used instead. The vertical axis is normalized per single nuclear muon capture process: the integration of the spectrum in whole energy region becomes $(1 - f_{\rm MC})/f_{\rm MC}$. This factor is 11.5 for carbon while 0.67 for aluminum. In the DIO spectrum normalized to unity, the yield from muonic carbon atom near the endpoint energy is almost factor 3 smaller than from aluminum since carbon nuclei is much lighter than aluminum. However, due to the factor above, the strength of the DIO background compared to the μ-e conversion becomes worth in carbon material. In order to suppress the DIO from carbon below 10^{-13}, the energy region to identify the signal should be $E_e > 101.5$ MeV/c if the detector resolution is 0.5 MeV/c, and $E_e > 102.0$ MeV/c if the detector resolution is 1.0 MeV/c. For the aluminum (or silicon) case, the sensitivity goal can be 10^{-14} and $E_e > 102.0$ MeV/c if the detector resolution is 0.5 MeV/c, but $E_e > 103.0$ MeV/c if the detector resolution is 1.0 MeV/c. If the energy resolution becomes larger than 2.0 MeV/c(r.m.s), the E_e should be 104 MeV/c, and the signal acceptance will become very small. Therefore, the energy resolution of the detector has to be better than 0.5 MeV/c.

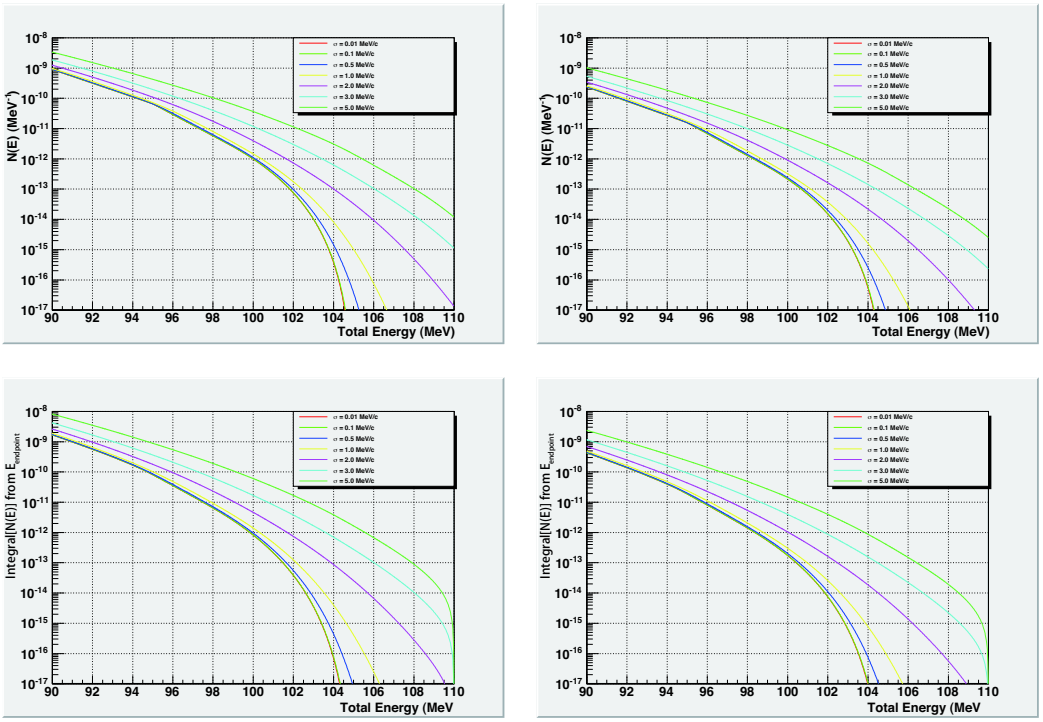

Figure 6.2: Total energy spectra of electrons from DIO in carbon and aluminum. Top left plot is a differential spectrum for muonic carbon, Top right plot is a differential spectrum for muonic aluminum, Bottom left plot is an integrated spectrum for muonic carbon, where the integration is from the energy of interest to the maximum energy. Bottom right plot is an integrated spectrum for muonic aluminum. Convolution spectra with gaussian distribution are shown in different colors. Please see the legends for the meaning of colors.

6.2 Simulated Detector Performance

In order to see the detector resolution, a Monte Carlo calculation of the magnetic spectrometer system was performed. Electrons with 105 MeV/c momentum were produced at the front of WC1 and the hit position in WC1–4 were recorded. Material of WCs are Kapton and the thicknesses are all 0.0715 mm. This thickness corresponds to 2.5×10^{-4} of the radiation length. Planer chamber with such a thickness actually built for MEG experiment, and are in operation in good condition[48]. The momentum fitting was performed by using a fourth-order Runge-Kutta integrator with the same magnetic field map used for the event generation. Spacial resolution of chambers were assumed to be 0.2 μm, and multiple scattering by WC2 and WC3 were considered by means of a breakpoint method. Figure 6.3 shows result of the track fitting. The momentum resolution is 0.32 MeV/c(rms), and the tracking efficiency (the fraction of the track result with the probability begin more than 0.05) is 86%. Therefore, the construction of the magnetic spectrometer system with 0.5 MeV/c momentum resolution for 105 MeV/c electrons is very realistic.

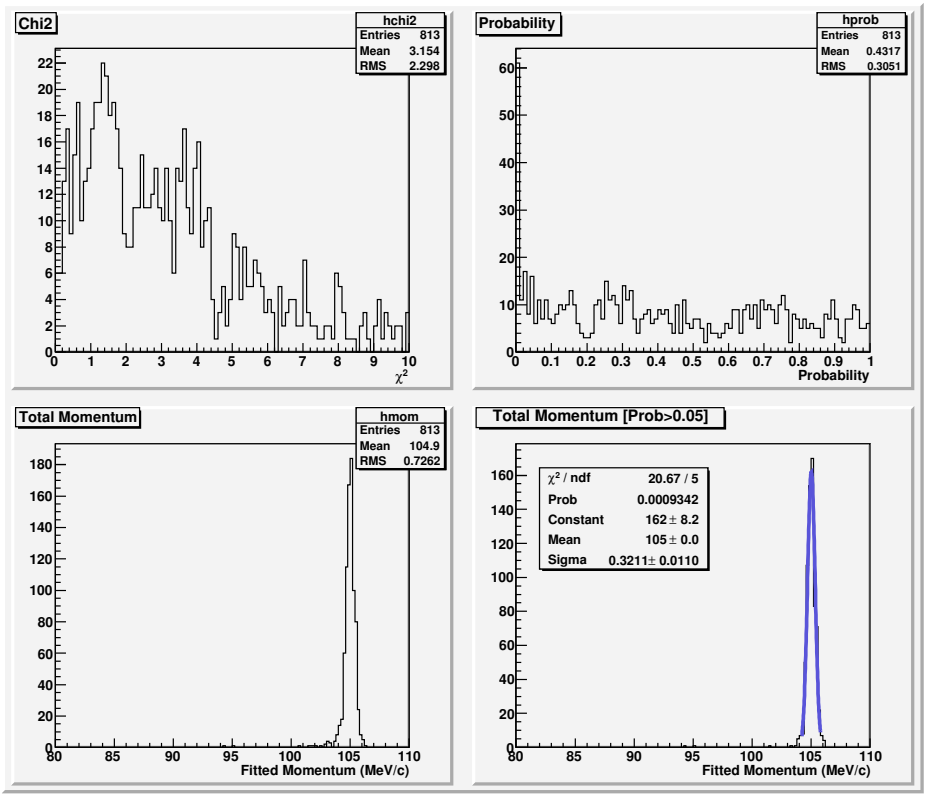

Figure 6.3: Track fitting result. Top left is χ^2 distribution. Top right is a probability distribution. Bottom left is a fitted momentum without any cuts. Bottom right is a fitted momentum after selection good probability.

6.3 Counter System

Two hodoscope counters will be used for trigger and particle identification. In order to minimize the material in front of the tracking chambers, both counters are located downstream of tracking chambers. The reasons why the material in front of the chamber should be avoided are as follows:

1. to minimize the energy loss and multiple scattering of signal electrons,
2. to minimize the probability of beam muons stopping in the material in front of tracker.

The first reason is very clear. The second reason may need explanation. There is negative muons contaminated in the electron beam about 1%. Some of those negative muons may scatter of the pillar of DSEPTUM during the prompt-burst, and enters to the detector with lower momentum. Some of them will stop in the plastic scintillator and produce Michel electrons in delayed timing. These Michel electrons will hit through the trackers If the counter is place in front of them, but wiped-out by magnet and do not hit WC1–2 if the counter is placed back of magnet.

If the number of prompt-burst hit is too many, the following things will happen:

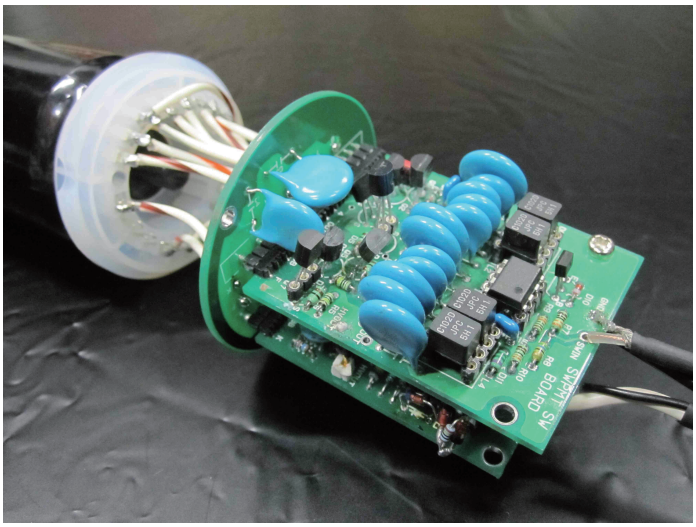

Figure 6.4: A photograph of the gating-grid circuit we developed.

1. delayed fluorescence from plastic scintillator will dominate in the delayed-time region and overwhelm the signal from the delayed charged particle hit,

2. instantaneous current load from dynodes in photomultipliers become too high and recharge up of the dynode voltage may take longer than the delayed-time region and the counter will be dead or lower-gain state during the measurement period.

We have a good experience operating plastic-scintillation counter under a prompt-burst condition in 2009. In 2009, a test experiment to measure the muonic atom formation rate was performed at Area D2. At that time, a counter system with gating-grid photomultipliers were used with 3k of prompt-burst. Figure 6.4 shows a photograph of the gating-grid circuit we developed. The gating-grid circuit raises high voltage of a focus grid and the 3rd dynode during a gate input is on. The gain of photomultiplier (PMT) during the gate-in is lower than the normal gain by factor 10^{-6}. Figure 6.5 shows snap shop of test counter signals taken at the time of the test measurement. Right after the gain of PMT came back to the normal, the baseline of the PMT signals showed sudden jump and slow decrease as time goes by. The amount of the baseline jump increases as the rate of prompt-burst increases. If the rate of prompt-burst is decreased, the amount of baseline jump decreases and eventually they became individual small pulses. The rate of the prompt-burst at the time of the test measurement was about 3k hits/pulse. When the gating-grid was turned off, the baseline jump became unacceptably high, and the PMT was not operational.

Now, there are individual pulses observed on the top of baseline curve, mostly in coincidences between two counters. These signals are from real hits of the charged particles. In order to separate the individual signals from the baseline, whole the waveforms were recorded by using waveform digitizers.

The analysis of the waveform was performed by the following steps:

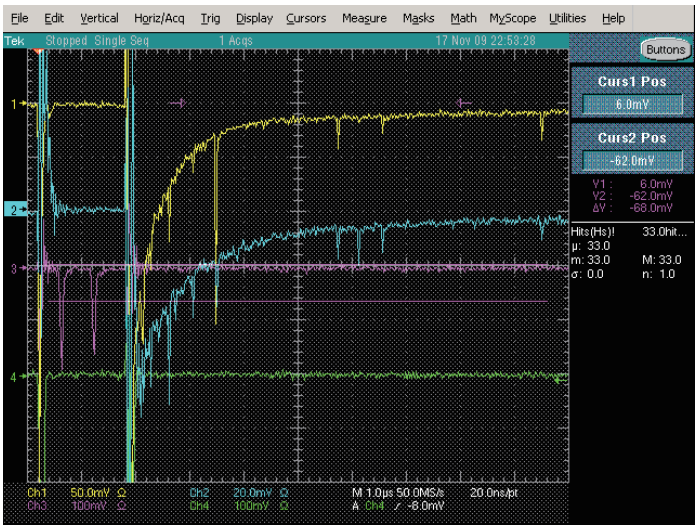

Figure 6.5: Snap shop of the waveform from gating-grid PMTs hit with prompt-burst. Yellow and light blue curves are both signals from gating-grid PMTs. They are stacked so that the beam particle should hit through them at the same timing. Purple curve is a signal from normal PMT but the light from plastic scintillator to PMT was decreased with ND filter. Disregards green curve. Two pulses observed in purple curve indicate the timing of two prompt-bursts.

1. identify the individual pulses by seeing the sudden change of waveform.
2. record the waveform value outside of the individual pulses as the pedestal.
3. average the pedestal waveforms over 100 waveforms to reduce the fluctuation.
4. subtract the pedestal waveform from each waveform.
5. set the signal threshold to identify the individual signals.
6. record the leading edge timing and the waveform integration of the individual pulses.

Figure 6.6 shows the integrated pulse area spectra. Each counter signal is tagged by the other counter signal. Valley between signal peak and pedestal noise is clearly observed. It means: despite of the baseline jump due to delayed fluorescence light, individual signals can be identified with 100% of efficiency.

Based on this experience, the delayed signals after several thousands of the prompt-burst can be detected by using the gating-grid PMT with waveform digitization technique. Above this level, we do not know if it works or not, yet. Therefore, the rate of the prompt-burst from each counter should be controlled at this level. Since the expected total number of prompt-burst in the μ-e conversion experiment is about 33k, the construction of the hodoscope will be easily realized by dividing the counter into more than 10 of segments.

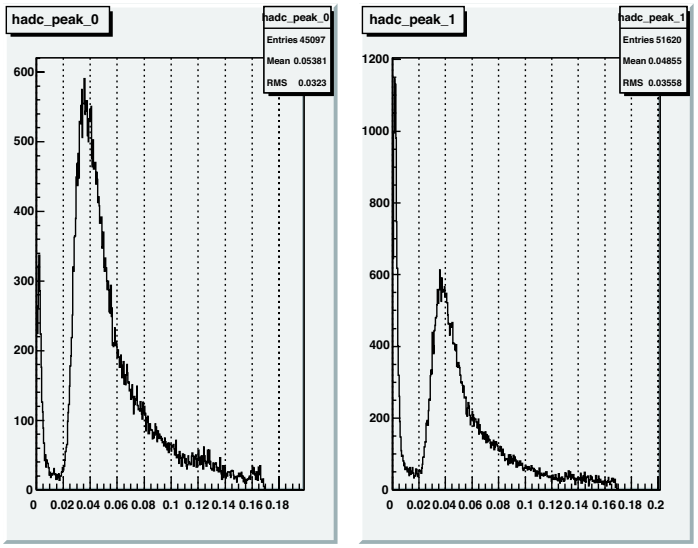

Figure 6.6: Integrated pulse area spectra for the 1st and 2nd counters. Left pane is the 1st counter tagged by the 2nd counter, and right pane is the 2nd counter tagged by the 1st counter.

6.4 Tracker System

In order to realize the experiment, the electron spectrometer should fulfill the following requirements. First, the momentum resolution should be better than 0.5 MeV/c(rms) in order to separate the μ-e electrons from the DIO electrons effectively, and thus, the intrinsic spacial resolution of the tracking detector should be a level of a few hundred μm assuming ≈ 0.4 T of bending field. Second, the tracking detector should be operational at a very high counting rate. As described in Chapter 4, approximately 33k particles per single beam bunch is expected to enter the detector region as a prompt burst. Thus the tracking detector should be designed to dedicate for such a strong irradiation environment. Therefore, adopting the drift chamber which consists of very small cell as a tracking detector is suitable to realize this experiment. In general, the use of a small gap between the anode plane and the cathode plane provides fast removal of the positive ions produced in the avalanche process, and hence, this allows reducing the collection time of the positive ions and increasing the rate capability of the device by reducing the space-charge effect. On the other hand, using small drift cell obviously results small primary ionization. This, however, can be compensated by adopting a high gas amplification or asymmetric cell dimension that will be discussed later as a further considerable option.

Schematic layout of present design of magnetic spectrometer is shown in Figure 6.1. The spectrometer consists of a simple dipole magnet (DB4) sandwiched by four sets of tracking stations (WC1–4). Each tracking station consists of two orthogonally placed planer drift chambers, and measures two dimensional position of the particle. There is a trigger hodoscope (BH1) and a time-of-flight hodoscope (BH2) located downstream of the spectrometer in order to reject off-timing muon backgrounds.

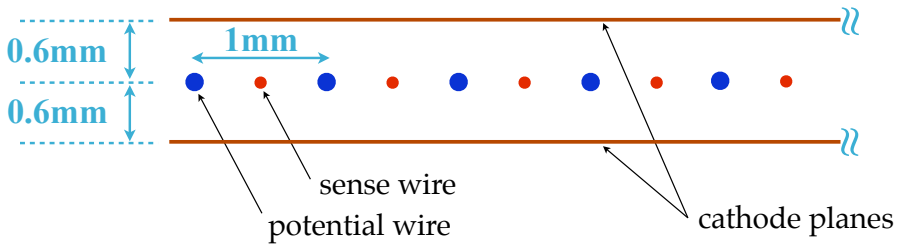

Figure 6.7: Schematic view of the cross-section of the drift chamber

Figure 6.7 shows the schematic view of cross-section of the present design of drift chamber. The anode plane consists of alternating thin 10 μm diameter sense wires and 20 μm diameter potential wires on a 500 μm spacing. The cathode plane is located only 600 μm away from the anode plane on both side in order to realize a very small drift cell as discussed above. The cathode plane is composed by 12.5 μm thick polyimide film with a few hundred nm thick aluminum or copper deposition.

The sense wire is connected to an embedded readout line through a decoupling capacitor and bifurcated to the high-voltage supply via a protection high-resistance, and applied positive voltage at a typical value of 1600 V. The mixture of 80% Ar and 20% C_2H_6 is adopted to have an enough fast drift velocity and no big gain modification at the expected environment.

Figure 6.8(a) shows the calculated field contour of the drift chamber, and Figure 6.8(b) shows the simulated drift lines (red solid line) in a drift cell with isochrones (green dot line) with 2 nsec interval.

The maximum rate of operation of this chamber is expected to be extremely high, approximately 33k particles will enter when a prompt burst comes. It reflects the effect of the fast evacuation of the positive ions through the small gap. This effect is illustrated in Figure 6.8(b). The major part of the positive ion charge (approximately 80%), created closed to the sense wires, is collected by the potential wires or cathode planes.

As mentioned above, however, adopting a small cell sets off a small number of primary ionization cluster, namely, a small signal. Thus a realistic signal-to-noise ratio should be carefully reviewed to guarantee the drift-chamber performances. Figure 6.9(a) shows simulated distribution of number of ionization clusters. Even a small number of clusters, an average of $\sim$14, are expected, this can be compensated by a high gas amplification. As shown in Figure 6.9(b), calculated Townsend coefficient is relatively large, and hence, it is easy to obtain a high gas amplification for this chamber, *eg.* $\gtrsim 10^4$. Assuming this size of primary ionization, gas amplification, and $\times$50 of preamplifier with a typical time constant of circuit *etc.*, approximately tens of volts of pulse height is expected. Thus, if $\sim$1 mV of noise level is realized, the signal-to-noise ratio should be good enough. Even the signal size is satisfactory,

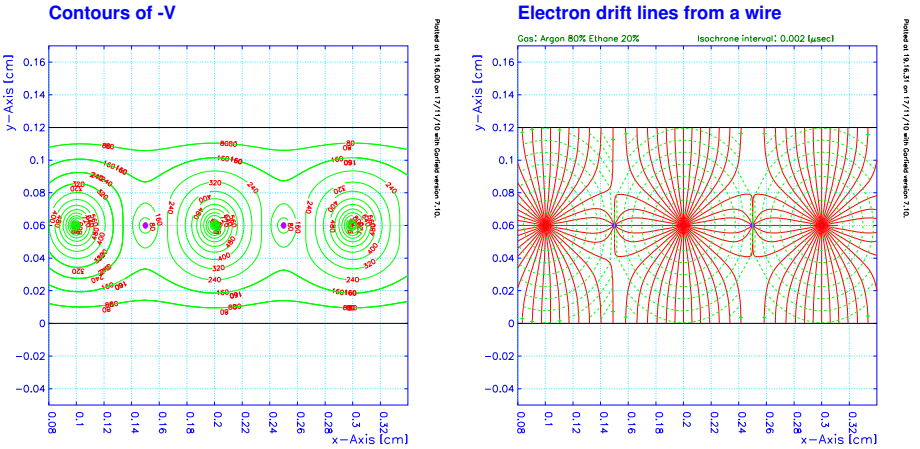

(a) Calculated field contour (b) Simulated drift lines and isochrons

Figure 6.8: Drift chamber simulation with the GARFIELD program (no magnetic field)

big-bang of electron avalanche caused by prompt burst should be taken into account carefully. As it was already explained in previous sections, two bunches of burst stand at the forefront of each beam train with a 600 nsec interval while each bunch has 33k particles within a 200 nsec pulse width. Assuming the calculated size of primary ionization and the factor of gas amplification, this prompt burst generates $\sim 2\times 10^{9}$ electrons which is corresponding to 3×10^{-10} Coulomb per wire, and hence, an expected instantaneous voltage depression is $\sim$0.1 V with a help of a few μF of buffer capacitor. In addition, involving a few pF of fast bypass capacitor helps to stabilize the voltage even if the prompt burst makes a big voltage depression.

We plan to read each of the sense wire with multistop TDCs. According to the present design, each plane consists of 400 sense wires, *ie.* 3200 channels are read in total. Approximately 2 nsec accuracy of leading-edge measurement is expected which is corresponding to $\sim$200 μm of bidirectional spacial resolution while calculated typical drift velocity is $\sim$9cm/μsec. The read out of cathode strip will be also considered.

Nonetheless, there is still a potential risk of wire breaking due to a huge amount of charge generation while the prompt burst. Additionally, even it is dedicated especially to be operational at the expected high counting rate, however, further considerable options are useful to ensure a fully operational detector. For this purpose, two options are under consideration; (A) **asymmetric drift cell** and (B) **switching-voltage scheme**.

The asymmetric drift cell has an asymmetric gap between the anode plane and the cathode plane, *eg.* 600 μm gap of one side and 3 mm gap on another side. Such an asymmetric cell allows a very short path for the positive ions which increases the rate capability, while a larger gap on the other side of the anode plane allows a sufficient number of primary electron-ion pairs to be generated. Figure 6.10(a) shows the simulated drift lines (red solid line) in an asymmetric drift cell with isochrones (green dot line) with 2 nsec interval. Fast evacuation of the positive ions through the

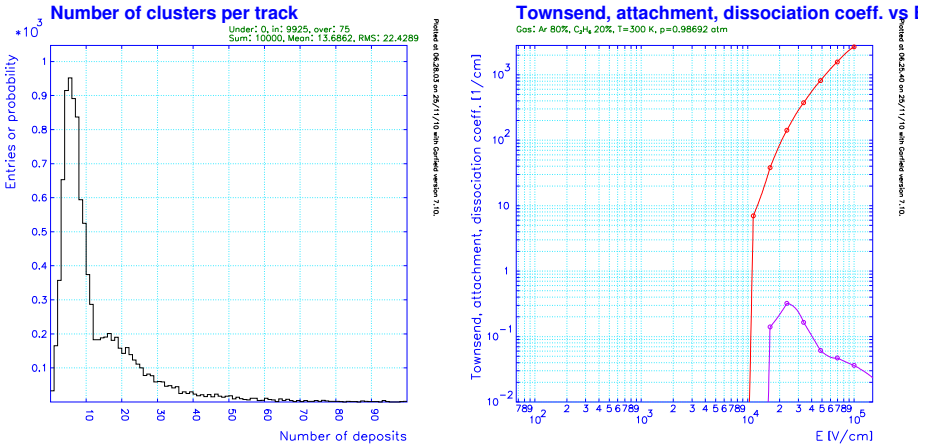

(a) Simulated number of clusters (b) Calculated Townsend coefficient, *etc.*

Figure 6.9: Drift Chamber simulation with the GARFIELD program (gas property)

lower small gap and enough wide ionization region in the upper big gap are shown. As shown in Figure 6.10(b), the number of cluster increases by a factor of 2.3 from the symmetric cell (Figure 6.9(a)). In fact, a similar idea was already demonstrated by some past developments [49] successfully. This idea helps a lot to compensate a small number of primary ionization due to small gap.

Even if the asymmetric drift cell is not enough to ensure a full operation, switching-voltage scheme will help. This scheme is assuming to have an enough fast switching high-voltage supply which allows to have a **blind period** of the detector operation. Data acquisition will open the integration window 300 nsec after the two prompt burst, and hence, it is not necessary to be operational during the two prompt burst. Thus the dedicated voltage supply which can realize to blind the prompt burst period is under development. It is not necessary to fall down the voltage completely; just reducing a few hundred volt is enough to suppress the gas amplification. According to the calculated Townsend coefficient (*cf.* Figure 6.9(b)), it is expected that the gas amplification is expected to be active at higher than 1kV, and thus, adopting 1.2-1.3kV of the operation voltage with 200 V of the switching voltage can realize such a scheme. Nonetheless, the asymmetric cell option should be realized for this scheme because 1.2-1.3kV is 300 V lower than the originally planned operation voltage.

6.5 Trigger and Data Acquisition System

As it was already described in the previous sections, signal waveforms from all the counters will be digitized and recorded. Because of the number of RCS extractions is only 25Hz, it is possible to record the waveform for all the extraction. The record length for a single extraction will be 20 μs, and start 10 μs before the extraction timing so that the signal before proton hitting the Muon Target will be also recorded for the

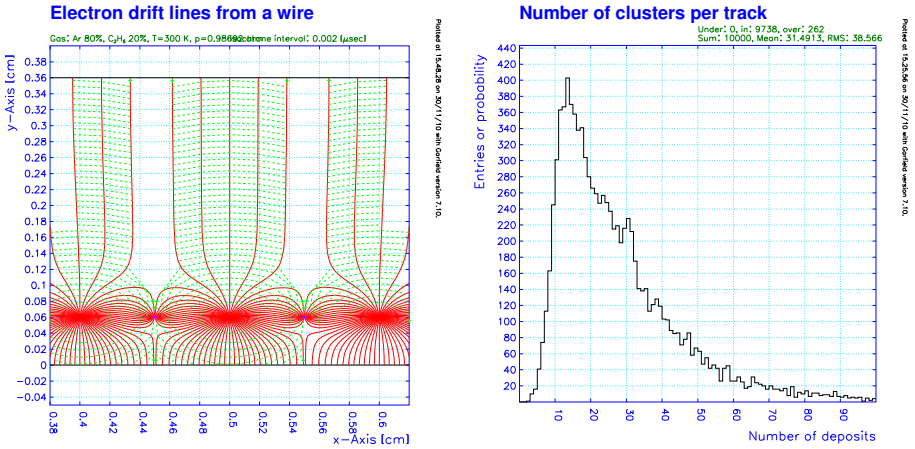

(a) Isochrons of asymmetric cell (b) Simulated number of clusters

Figure 6.10: Simulation of the asymmetric drift-cell option

Table 6.2: Data size from each detector components.

Component	No. of channels	f_{sampling}	Size per shot
Hodoscope	50	500MHz	0.5MB
Anode	3200	—	0.2MB
Cathode	400	100MHz	0.8MB

background study. The number of channels to be recorded will be 50 maximum.

Signal from the anode wire of the wire chambers will be discriminated and the timing is recorded by multiple stop TDC. The number of anode channels to be recorded is 3200. The timing resolution of the multiple stop TDC should be 2 nsec. Signal waveforms from cathode strips of wire chambers could be digitized and recorded. Based on the test measurement in 2009, the number of delayed hits per single RCS extraction is expected to be much less than 1[1]. The data size per single extraction will be 1.5MB per shot, and 37.5MB/s, and it is fairly easy to handle this level of data stream.

The total size of data will be about 800TB for 2×10^7 s of data taking. The most of data will be just baselines without signal hits. Therefore, non-distractive data suppression will be very effective, and will be more than factor 10 of data size reduction could be anticipated. The final data size will be a level of 100TB, and which is well within the available storage size these days.

[1]They are mostly coming from Michel e^- from μ^- stopped in the middle of beam line.

Chapter 7

Sensitivity and Backgrounds

Sensitivity of the measurement depends on the choice of configurations. We put the highest priority to perform the measurement at H-line with the SiC production target, that gives the best sensitivity. However, in order to illustrate the advantage of performing the measurement at H-line, the expected sensitivity at the other configuration, such as D-line, will be also discussed in the following sections.

The most serious source of backgrounds is the one caused by late-arriving protons. The amount of the late-arriving proton has to be suppressed by factor 10^{-17}. Since the proton beam is fast-extracted from RCS to MLF at once, and the kick angle is much larger than the physics aperture of the RCS, it is very hard to evaluate the amount of the late-arriving protons from theory of beam dynamics. It is very important to monitor the effect of the late-arriving protons along with the physics data acquisition.

7.1 Physics Sensitivity

Single event sensitivity to μ-e conversion process is expressed by the following equation:

$$S = \frac{1}{N^{\mu}_{\rm obs}}, \tag{7.1}$$

where $N^{\mu}_{\rm obs}$ is a total number of muonic atoms observed. The $N^{\mu}_{\rm obs}$ can be expressed as:

$$N^{\mu}_{\rm obs} = R_{\pi^-} \times f_{\pi^- \to \mu^- {\rm stop}} \times f_{\rm C} \times f_{\rm MC} \times A_{\mu-e} \times T\,, \tag{7.2}$$

where $R_{\pi^-} \times f_{\pi^- \to \mu^- {\rm stop}}$ is a μ^- stopping rate per second, $f_{\rm C}$ is the atomic capture rate on the specific atomic species of interest constituting a compound or a gaseous mixture, $f_{\rm MC}$ is a fraction of μ^- that goes to the muon nuclear capture process, $A_{\mu-e}$ is the total acceptance for μ-e electrons, and T is a time length of the measurement. The factor $f_{\rm C}$ was estimated by using the Fermi-Teller Z law[34], in which the atomic capture rate is claimed to be proportional to the nuclear charge of the atom. There are several reports indicating the shift from the Fermi-Teller Z law, but the shifts are

only a level of a few of 10% for light nuclei[35]. In this proposal, the Fermi-Teller Z law was simply used.

The factor $f_{\rm MC}$ is the fraction of the nuclear capture process. It increases as the atomic number increases since the overlap of the muon wave function with the nuclei increases as the Coulomb potential becomes deeper. There are both experimental and theoretical studies about $f_{\rm MC}$[37, 40].

The $A_{\mu-e}$ can be further broken down to the following expression:

$$A_{\mu-e} \;=\; A_{\rm beamline} \times A_{\rm detector} \times A_{\rm tracking} \times A_{E_e\text{-cut}} \times A_{\text{time-window}}\,. \qquad (7.3)$$

These factors were estimated by using the combination of Geant4 and G4Beamline simulation for D-line. As for H-line, the result of D-line was simply scaled by using the design parameter of H-line obtained by the optics calculation.

At first, the μ^- stopping positions in the target, where the μ^- is produced by 3-GeV protons, was calculated by using Geant4 with QGSP_BERT_HP hadron code. Then, these μ^- stopping positions are fed to yet another Geant4 simulation code to produce μ-e electrons isotropically. The typical number of μ^- stops in the target in the simulation was only level of 1000 due to the limit coming from the calculation speed of the computer. Ten thousands of μ^--e^- electrons were produced per each vertex so that the beamline transmission efficiency (typically 10^{-3} level) can be properly estimated for each vertex. The electrons emerging out of the target material were further tracked by using G4Beamline through D-line and detector down to the final hodoscope. Figure 7.1(a) shows μ-e momentum spectrum at the entrance of the D-line. Because of the energy loss in the Muon Target material, the distribution of the spectrum becomes broad and there is a long tail in the lower momentum region. Figure 7.1(b) shows μ-e momentum spectrum at the exit of the D-line. Electrons with momentum lower than 95 MeV/c are not able to transport through the D-line.

The $A_{\rm beamline}$ is a ratio between the electrons entering the detector and the electrons produced in the target. It includes all the effect from electron energy loss in the target, beamline acceptance, beamline momentum bite and so on. The $A_{\rm detector}$ is the ratio between the particle hit the final hodoscope and the one entering the detector.

The $A_{\rm tracking}$ and the $A_{E_e\text{-cut}}$ were estimated after performing the fourth-order Runge-Kutta track fitting. Figure 7.2 shows the result of the track fitting. The performance of the track fitting itself was already described in Chapter 6. The $A_{\rm tracking}$ is mostly limited by the track quality cut, in which the track probability is required to be more than 5%. Those event rejected might be suffered from the large angle scattering by the chamber material. This effect might be treated in much better way by using double Gaussian approximation to the multiple-scattering angle distribution in the future, and the $A_{\rm tracking}$ could be higher than the current value. The momentum resolution of the track fitter itself is 0.36 MeV/c, thus the distribution of Fig. 7.2 is dominated by the energy loss of electrons in the target and the beamline acceptance.

The $A_{E_e\text{-cut}}$ depends on the E_e cut threshold. The threshold was determined to suppress the DIO background lower than the S.E.S level. It is about 102.5 MeV/c as will be described in the next section.

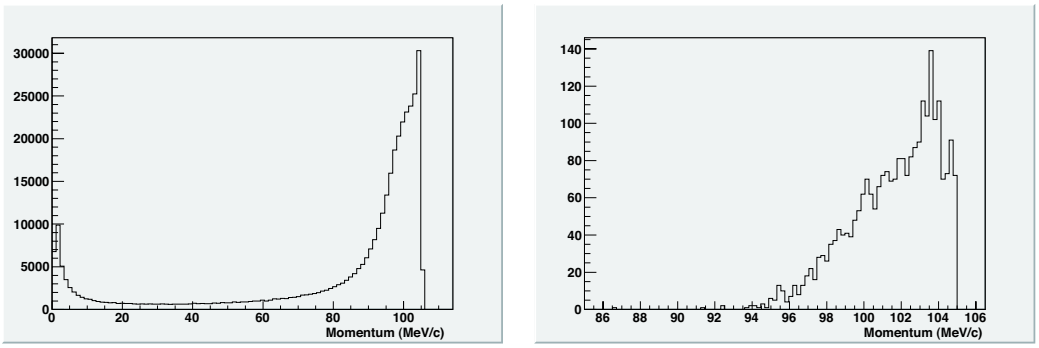

(a) At the beamline entrance. (b) At the beamline exit.

Figure 7.1: Electron momentum spectra calculated with Geant4 and G4Beamline for D-line and the rotating graphite target.

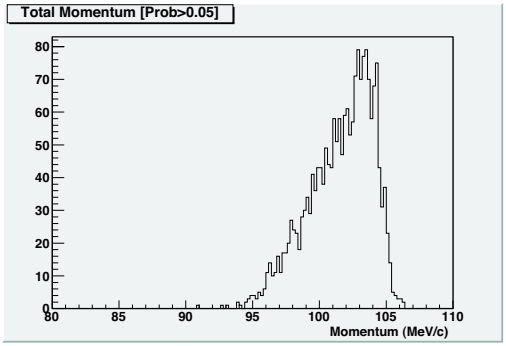

Figure 7.2: Electron momentum spectra obtained by the track fitting to the event in the Fig. 7.1(b).

Table 7.1 summarizes the potential sensitivity for measurements at D-line. Three different configurations are listed together. The first is to use the existing target and beamline as it is, the second is replacing the DSEPTUM magnet with much larger aperture, and the third is replacing the material of the Muon Production Target with SiC and enlarge the size of ring by 20 mm in addition to replacing the DSEPTUM.

The single event sensitivity of the 1st option is about the same to the current upper limit 7×10^{-13} for gold given by SINDRUM-II[17]. It is not significant at all. The third configuration provides almost one-order-of-magnitude improvement over the SINDRUM-II result. If we consider the difference of nuclei, and the sensitivity to the new physics can be totally different for the different nuclei[41], this result improves the measurement for light nuclei almost two orders of magnitude[15]. However, it is always better to try to maximize the experimental sensitivity as much as reasonably achievable.

From that point of view, the measurement at H-line will give us the maximum sensitivity. Table 7.2 shows expected sensitivities for the measurement at H-line with several different configurations of target assembly. In making this table, we assumed

Table 7.1: Breakdown of physics sensitivity for the measurement at D-line.

	as it is	new DSEPTUM	SiC target
Muon Target Material	C	C	SiC
$R_{\mu^-\text{-stop}}$ (/sMW)	10×10^9	10×10^9	15×10^9
$f_{\rm C}$	1.0	1.0	0.7
$f_{\rm MC}$	0.08	0.08	0.66
$A_{\mu-e}$			
$A_{\rm beamline}$	0.025%	0.05%	0.05%
$A_{\rm detector}$	97%	97%	98%
$A_{\rm tracking}$	81%	81%	81%
E_e cut threshold (MeV/c)	101.0	101.0	102.0
$A_{E_e\,\rm cut}$	63%	63%	60%
$A_{\rm time\text{-}window}$	0.75	0.75	0.49
T (s)	2×10^7	2×10^7	2×10^7
S.E.S	6.5×10^{-13}	3.2×10^{-13}	6.6×10^{-14}
$N_{\rm DIO}$	2.7×10^{-13}	2.7×10^{-13}	2.4×10^{-14}

the improvement of the beamline acceptance by factor 10 $\simeq$ 110 msr/10 msr based on the discussion in Chapter 4. It is quite obvious that the measurement at H-line will provide the best performance. The configuration in the last column in Table 7.2, measurement at H-line with SiC target, is the one we aim to realize.

7.2 Background

There are two major sources of backgrounds: muon decay-in-orbit, and prompt backgrounds. Cosmic ray induced backgrounds will be also discussed.

7.2.1 Muon Decay-in-Orbit Backgrounds

When a muonic atom is formed, the muon come to its ground state very quickly. Then, it either be captured by a nucleus with emitting a neutrino (nuclear muon capture) or decays in orbit (DIO). These two processes are concurrently happening, and the total width of the muon reaction becomes wider than the width of the muon in free space. For instance, about 92% of muons decay in orbit for an carbon target. Their energy spectrum in the energy region lower than 52.5 MeV mostly resembles the Michel spectrum of ordinary muon decays, but a high energy tail exists due to nuclear recoils, and it extends up to the same energy as the μ-e conversion signal. Thus, the electrons from DIO become one of potential background sources.

The energy spectra of DIO electrons are studied with nuclear-recoil energy taken into account[24]. With the approximation of a constant nuclear-recoil energy, the electron spectrum with an expansion in powers of the electron energy (E_e) at the

Table 7.2: Breakdown of physics sensitivity for the measurement at H-line.

Target Configuration	Graphite	large Graphite	large SiC
Muon Target Material	C	C	SiC
$R_{\mu^-\text{-stop}}$ (/sMW)	10×10^9	15×10^9	15×10^9
$f_{\rm C}$	1.0	1.0	0.7
$f_{\rm MC}$	0.08	0.08	0.66
$A_{\mu-e}$			
$A_{\rm beamline}$	0.25%	0.25%	0.25%
$A_{\rm detector}$	97%	98%	98%
$A_{\rm tracking}$	81%	81%	81%
E_e cut threshold (MeV/c)	102.0	102.0	102.5
$A_{E_e\,\rm cut}$	49%	60%	52%
$A_{\rm time\text{-}window}$	0.75	0.75	0.49
T (s)	2×10^7	2×10^7	2×10^7
S.E.S	8.3×10^{-14}	5.7×10^{-14}	1.5×10^{-14}
$N_{\rm DIO}$	5.5×10^{-14}	5.5×10^{-14}	0.9×10^{-14}

Table 7.3: Numerical values of D, E, F and the energy of $\mu^- - e^-$ conversion electrons.

Material	Z	$D(\times 10^{21})$	$E(\times 10^{21})$	$F(\times 10^{21})$	$E_{\mu e}$ (MeV)
C	6	0.280	0.700	2.00	105.10
Al	13	0.388	1.03	2.50	104.99
Si	14	0.495	1.35	3.00	104.93
Ti	22	2.08	6.36	14.00	104.27

end-point energy is given by

$$N(E_e)dE_e = \left(\frac{E_e}{m_\mu}\right)^2 \left(\frac{\delta_1}{m_\mu}\right)^5 \left[D + E \cdot \left(\frac{\delta_1}{m_\mu}\right) + F \cdot \left(\frac{\delta}{m_\mu}\right)\right] dE_e, \tag{7.4}$$

where $\delta = E_{\mu e} - E_e$, $\delta_1 = E_{\mu e} - E_e - E_{\rm rec}$ and $E_{\rm rec}$ is the nuclear-recoil energy given by $E_{\rm rec} = E_e^2/(2M_A)$. The coefficients D, E and F as well as the end-point energy are calculated as shown in Table 7.3 by interpolating parameters given in [24]. It should be stressed that the spectrum falls off sharply as the fifth power of δ_1 towards its end-point, $(\delta_1)^5 \approx (E_{\mu e} - E_e)^5$.

Since the Eq.(7.4) is valid only near the endpoint of the spectrum, the numerical values of the spectrum shapes of DIO electrons compiled by Watanabe *et al.*[25] was used for the lower energy region. Both the spectra are connected smoothly at around $E_e \simeq 100$ MeV. The total energy spectra of DIO electrons calculated by the method explained above was already shown in Fig. 6.2 for both carbon and aluminum cases.

In order to evaluate the background contribution from DIO electrons, the the-

Table 7.4: Expected DIO backgrounds assuming the detector resolution being a single Gaussian with $\sigma = 0.5$ MeV/c.

	C	Al	SiC
$E_e > 100.0$ MeV	9.5×10^{-13}	2.0×10^{-13}	4.2×10^{-13}
$E_e > 101.0$ MeV	2.7×10^{-13}	5.5×10^{-14}	1.2×10^{-13}
$E_e > 102.0$ MeV	5.5×10^{-14}	1.1×10^{-14}	2.4×10^{-14}
$E_e > 102.5$ MeV	2.1×10^{-14}	4.1×10^{-15}	9.2×10^{-15}

oretical DIO spectra were convoluted with the response function of the momentum measurement. The response function is assumed to be a single Gaussian, and several cases of the tracker resolutions were considered. Then, the total amount of DIO is normalized to the nuclear capture process since the μ-e conversion process is normalized to the nuclear capture process too:

$$R(\mu^- + \mathrm{A[N,Z]} \to e^- + \mathrm{A[N,Z]}) \;=\; \frac{\Gamma(\mu^- + \mathrm{A[N,Z]} \to e^- + \mathrm{A[N,Z]})}{\Gamma(\mu^- + \mathrm{A[N,Z]} \to \nu_\mu + \mathrm{A[N,Z\text{-}1]})}\,.$$

For examples, in carbon target, the ratio between the muon nuclear-capture process and DIO is 0.08:0.92, that means there will be $0.92/0.08 = 11.5$ times of DIO per a single muon nuclear-capture process. It is only factor 0.67 and 0.66 for aluminum and silicon, respectively. In the Fig. 6.2 shown in the Chapter 6, differential and integral spectra for several different tracker resolutions were shown. Table 7.4 summarizes the expected DIO backgrounds for several different energy regions. The DIO is certainly one of potential backgrounds, but it can be controlled at a cost of sensitivity loss due to raising E_e.

7.2.2 Prompt Backgrounds

The most dangerous source of background is the prompt electrons coming from late-arriving protons. Based on the knowledge we obtained in the beam test in 2009, the expected number of prompt beam particles in the momentum region 100–105 MeV/c is about 5×10^{-7} per proton on the Muon Production Target for D-line. The total number of on-timing protons on the Muon Production Target for 1MW operation of J-PARC RCS for 2×10^7 s of the running time is 4×10^{22}, and there should be about 2×10^{16} of prompt electrons produced. In order to suppress number of these events less than 1, the probability of the late-arriving protons in the detector time window should be 5×10^{-17} of the on-timing proton. Now, this requirement seems to be extremely difficult at the first sight, but it is not clear yet.

It is note worth that the mechanism of producing the off-timing protons in this experiment is totally different from that of COMET[21]. In COMET, a bunched slow extraction will be used to produce pulsed proton beam. RF buckets in the MR will be kept on during the extraction period, which is about 1 second, and the beam in the MR will be gradually moving towards the resonance. Part of the beam particles which

have larger betatron amplitude are hit the betatron resonance and move toward the outside of the beam packets, and the orbit of those halo beam will be bent by septum magnets towards the experimental area. Parts of the beam will be scattered off the septum foil, and stay in the MR to degrade the time structure of proton pulse. There will be also residual protons sitting in the "empty buckets", and they are source of off-timing protons.

On the other hand, in DeeMe, proton beam in RCS will be fast-extracted at once by kicker magnet system. After extracting the beam from the RCS, the kicker magnets fall down very fast so that the residual protons in the first bucket would feel only 10% of the full excitation magnetic field. Figure 7.3 illustrate this situation. In addition, the acceptance of the extracted beamline from RCS has been designed so as to be located outside of the physical aperture of RCS. This is illustrated in Fig. 7.4. The ring collimator aperture is 324πmm·mrad, and the extraction aperture is the same pulse additional 9 mm for the safely margin[50]. The beam emittance will be 81πmm·mrad for the core[51]. This is totally different from the design of J-PARC MR, where the fast extraction acceptance of MR is 19.5π mm·mrad while the beam emittance is 5π mm·mrad but the collimator aperture is 54π mm·mrad. Such design of RCS was originally motivated to reduce the beam loss during the extraction, but it is also beneficial to reduce the late-extracted beam. Even if there is beam halo in the RCS ring, any particles in the halo will hit the collimator before accidentally extracted from the RCS ring.

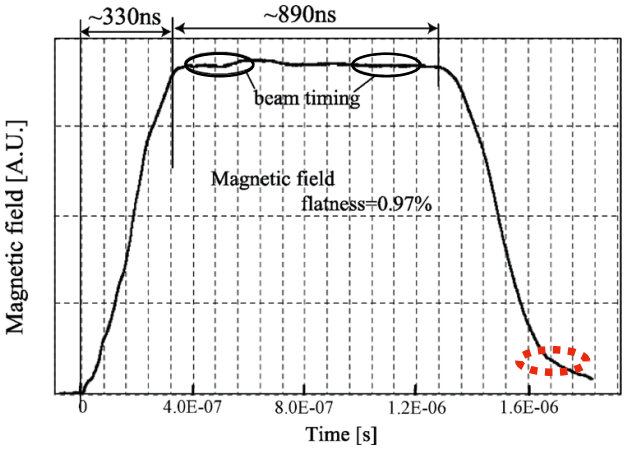

Figure 7.3: RCS extraction kicker timing. Red dotted ellipse shows a position of the 1st RF bucket after a turn-around in the RCS. The plot was taken from [52].

This can be partially monitored by looking at the secondary beam activities in MLF before the extraction time. Figure 7.5 shows waveforms from plastic counters located at Area D2 during the test experiment in 2009. There is no particles observed in the time region before the extraction ($< 10.5\,\mu$s). After accumulating more than 2×10^5 of the extraction events, no hits before the extraction time was observed. This implies the probability of the accidental extraction of the beam from RCS during the kickers being off is less than 10^{-9}, and it is statistics limited upper bound.

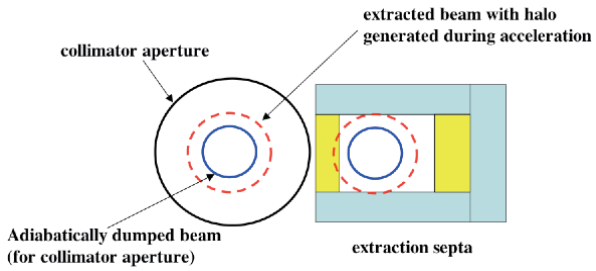

Figure 7.4: Relation between the beam size, the collimator and the extraction aperture of J-PARC RCS. This illustration was taken from [53].

The rate of the late-arriving protons should be less than one per 10 seconds, and this is totally outside of any monitors currently equipped in the RCS. It is also difficult to monitor it by using a simple counter coincidence since there will be delayed electrons coming from muon Michel decays, where muons stop in the counter. The only way to measure it is to momentum analyze the electrons and reject Michel decays, which is actually the same to the proposed measurement to search for μ-e conversion.

Figure 7.6 shows the momentum spectrum of the prompt electrons. The slop above 50 MeV is gentle and there is no structures in the spectrum. The change of the spectrum from 100 MeV/c to 110 MeV/c is only 10%. In the proposed experiment, the momentum region above 105 MeV/c will be monitored simultaneously. The integrated acceptance of D-line above 105 MeV/c is about the same to that of the signal region (100–105 MeV/c) as it can be seen in the Fig. 4.4(b). Therefore, it is possible to monitor the prompt background at the same level to the μ-e signal. In order to improve this situation, DSEPTUM should be modified to have much wider horizontal aperture. Then, the acceptance of the higher momentum region will be about doubled.

As it was already mentioned, the quick beam test showed that the probability of off-timing protons is less than 10^{-9}. From the same test, we obtained the probability of late-arriving protons begin less than 10^{-6}, where the measurement was limited by the background coming from Michel-decay electrons[54]. Therefore, the exact value of the rate of the late-arriving proton is still unknown. Please note that even if it does not fulfill our requirement, there are several ways to improve it. For examples, it would be possible to scrape the halo of proton beam before the extraction by using bump magnets in RCS. The extra kicker could be place between RCS and MLF to clean up the late-extracted particles. These kickers could be treated as spares to the main kicker system, then there would be no extra cost from our funding. The study for understanding the late-arriving protons from RCS is preferable. But, it should be noted that the background coming from the late-arriving protons will be monitored during the data taking.

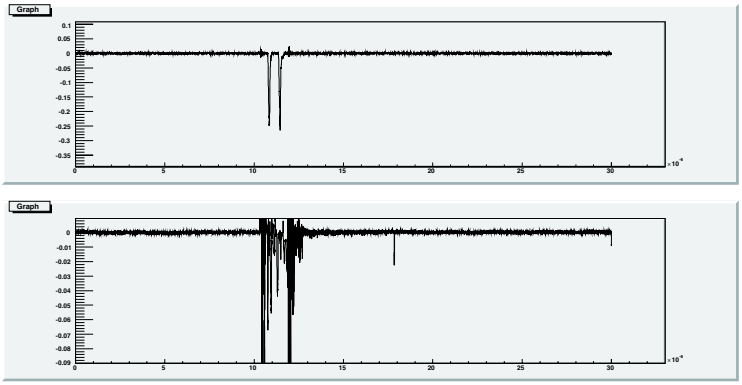

Figure 7.5: A snap shot of signal waveforms recorded during the beam test in 2009. Upper waveform is the normal photomultiplier and the two peaks corresponds to two proton pulses from RCS. Lower waveform is from gating-grid PMT, and the PMT gain is sensitive enough to see single pulses as seen around $t = 18\,\mu$s. Please note that this particular pulse was identified as a noise since there is no hit in the other counters in coincidence. Noises between 10–13 μs are from gating circuit and not from the real particles. There are no hits before $t = 10.5\,\mu$s.

7.2.3 Cosmic Ray Backgrounds

The cosmic-ray induced electrons could be a source of background, but there is an advantage in the proposed experiment regarding to the cosmic-ray induced background. The duty factor of the detector live time is only an order of 10^{-4}. In the COMET/Mu2e, where the duty factor is almost 1, the cosmic-ray veto is needed to reduce the cosmic-ray induced background by factor 10^{-4}. In the proposed experiment, there is no cosmic-ray veto counters, thus the expected number of cosmic-ray induced background will be 10^4 times larger per detector-live time, but it will be compensated by the duty factor. In addition, the sensitivity goal is two orders of magnitudes larger than COMET/Mu2e. Therefore, the cosmic-ray induced backgrounds will be small

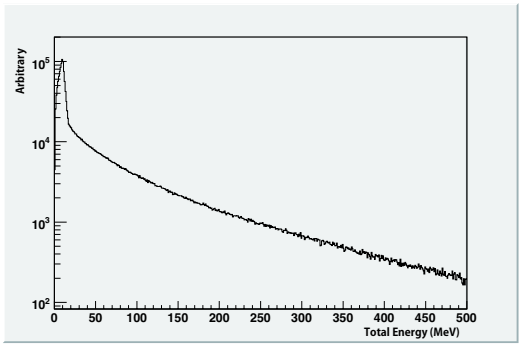

Figure 7.6: Total energy spectrum of prompt electrons produced by 3-GeV protons hitting graphite target.

enough.

7.2.4 Neutron Induced Backgrounds

High-energy neutrons will be produced at the neutron target, and the part of them will flight back to the Muon Target, and produce 100-MeV electrons. The kinetic energy of neutron has to be larger than 100 MeV in order to produce the 105-MeV/c electron. The velocity of such neutron is faster than 0.41 of the speed of light. The distance between the Muon Target and the Neutron Target is 33 m, thus the 100-MeV neutron will take 260 nsec from the Neutron Target to the Muon Target. Since the primary proton takes 115 nsec from the Muon Target to the Neutron Target, the neutron induced background will be delayed by 400 nsec if it exists. The neutrons with much higher energy will take shorter time.

The detailed study should be done with well established neutron code such as MCNP. However, it should be noted that the background can be rejected by moving the detection time window if necessary.

Chapter 8

Cost and Schedule

8.1 Cost

The cost estimate is shown in Table 8.1.

The construction of H-line and replacing the production target with SiC material for the maximum sensitivity will cost 16 Oku-Yen. However, please note that the 15 Oku-Yen is for the construction of H-line, and the H-line is not exclusively for this program. Many other physics programs, such as muon $g-2$, muonium hyper fine splitting measurements, muonium-antimuonium conversion search and so on, can be performed by using this H-line. The additional component only used for this program is the kicker system and modification to HS1 to enlarge the bore. After finishing the program, the area could be used for other surface-μ^+/cloud-μ^- experiments. Therefore, the construction cost for H-line has to be borne by the facility.

The cost for the detector construction is about 1 Oku-Yen. Since the specification of the spectrometer magnet is very common, the possibility to procure a secondhand magnet from outside such as TRIUMF will be seriously considered. The modification of the material of the muon target is only for this program. If the construction of H-line is delayed, the first measurement could be performed at D-line before moving to H-line. In that case, the modification of D-line will cost 70,000 kJPY in addition. In the case of measurement at D-line, it will cost 1.7 Oku-Yen in total. It is within the framework of the Grant-in-Aid for Scientific Research.

8.2 Schedule

The keys to the success of the program are:

1. acceptance of the secondary beamline,

2. suppression of the late-arriving protons from RCS.

The aim of the experimental group is to obtain the significant physic result within 5 years. In order to achieve the goal, we firstly concentrate on the design and construction of H-line, and the evaluation of the late-arriving protons. Then, at around

Table 8.1: Cost Estimate.

Item	Cost (kJPY)	Note
	Detector	
Spectrometer Magnet	(30,000)	Reuse the existing magnet.
Hodoscope	10,000	
Tracking Chamber R&D	3,000	
Tracking Chamber	50,000	Including frontend
Readout Backend	10,000	
Sub Total	*73,000*	
	Muon Target Modification	
SiC Target	30,000	
	H-line Construction	
HS1	400,000	
HS2–5	300,000	
HB1	50,000	
HB2–4	90,000	
Quadruples	50,000	
Kicker Magnets	60,000	
Kicker Power supply	160,000	
Vacuum	30,000	
Magnet Power supplies	300,000	
Install	40,000	
Sub Total	*1,480,000*	
	D-line Modification	
D-line kicker PS modification	50,000	
DSEPTUM modification	20,000	
Sub Total	*70,000*	

the end of 2012, the progress would be reviewed. If the realization at the H-line will be delayed, the first measurement would be performed at D-line, and the detector will be moved to the H-line afterward.

Chapter 9

Summary

We propose to search for the $\mu^- - e^-$ conversion in nuclear field at J-PARC MLF with a sensitivity of 10^{-14}, two orders of magnitude below current limits.

A CLFV signal may be seen in near future by experiments which improve the current limits. It is conceivable that the CLFV signal lies waiting to be discovered right under the current limit. A new experiment searching for $\mu^- - e^-$ conversion process at the 10^{-14} level would be a highly competitive addition to the field.

The experiment will be conducted by using the muon beam provided at MLF. Our intention is to realize the experiment in a timely manner by making a use of the MLF muon target system as a muon-stopping target to form muonic atoms, and the muon beam line with kicker to suppress the detector rate.

The muonic atom formation rate in the rotation muon target in MLF is as high as 10^{10}/sec/MW. If a large-acceptance high-momentum electron beamline is built as H-line, the single event sensitivity will be 1.5×10^{-14} for 2×10^7 sec of physics run. The proposed H-line is compatible with other muon experiments such as muon $g-2$, muonium hyper fine splitting measurement, muonium-antimuonium conversion, and so on.

The most serious source of backgrounds would be from the late-arriving protons from RCS. The amount of having such protons within the measurement time window has to be suppressed less than 10^{-17} of the number of main protons. Although it is very unlikely to having the late-arriving protons from RCS due to the extraction scheme of the RCS, dedicated studies would be very helpful. Since it will be monitored in the main measurement, we can still go for the physics run without full understanding of the suppression factor.

The cost that needed only for this experiment is about 1 Oku-Yen. The construction of H-line is needed for the maximum sensitivity, but the beamline can be used for many other fundamental muon science programs.

We would like to ask KEK for supports in the development of the pulsed proton beam with a good suppression on the late-arriving protons and H-line construction.

Chapter 10

Acknowledgement

The development of this expeirmental idea was partially supported by the Ministry of Education, Science, Sports and Culture, Grant-in-Aid for Exploratory Research, 21654034, 2009–2010.

Bibliography

[1] V. Barger, D. Marfatia and K. Whisnant, Int. Jour. Mod. Phys. E **12** 569 (2003).

[2] A. de Gouvêa, in *NEUTRINO FACTORIES AND SUPERBEAMS, 5th International Workshop on Neutrino Factories and Superbeams, NuFact03*, edited by A. Para (American Institute of Physics, Melville, New York), p. 275 (2004).

[3] J. Hisano *et al.*, Phys. Lett. B **391** 341 (1997); **397** 357(E).

[4] J. Hisano *et al.*, Phys. Rev. D **58** 116010 (1998).

[5] J. Hisano and D. Nomura, Phys. Rev. D **59** 116005 (1999).

[6] F. Borzumati and A. Masiero, Phys. Rev. Lett. **57** 961 (1986).

[7] R. Barbieri and L.J. Hall, Phys. Lett. B **338** 212 (1994).

[8] R. Barbieri *et al.*, Nucl. Phys. B **445** 219 (1995)

[9] G. Isidori *et al.*, Phys. Rev. D **75** 115019 (2007)

[10] G. W. Bennett *et al.* (Muon (g-2) Collaboration), Phys. Rev. Lett. **92**, 161802 (2004)

[11] R. Kitano *et al.*, Phys. Lett. B **575** 300 (2003).

[12] W.J. Marciano, T. Mori, and J.M. Roney, Annu. Rev. Nucl. Part. Sci **58** 315 (2008).

[13] M.L. Brooks *et al.* (MEGA Collaboration), Phys. Rev. Lett **83** 1521 (1999).

[14] U. Bellgardt *et al.*, Nucl. Phys. B **229** 1 (1988).

[15] C. Dohmen *et al.*, Phys. Lett. B **317** 631 (1993).

[16] P. Wintz *et al.*, in *Proceedings of the First International Symposium on Lepton and Baryon Number Violation*, edited by H.V. Klapdor-Kleingrothaus and I.V. Krivosheina, (Institute of Physics Publishing, Bristol and Philadelphia), p.534, unpublished (1998).

[17] W. Burtl *et al.* (The SINDRUM II Collaboration), Eur. Phys. J. C **47** 337 (2006).

[18] J. Adam *et al.* (The MEG Collaboration), Nucl. Phys. B **834** 1 (2010).

[19] R. Sawada, *presentation at ICHEP 2010*

[20] M. Blande *et al.* JHEP05 013 (2007).

[21] COMET Collaboration, "Conceptual Design Report for Experimental Search for Lepton Flavor Violating μ^--e^- Conversion at Sensitivity of 10^{-16} with a Slow-Extracted Bunched Proton Beam (COMET)", KEK Report 2009-10 (2009).

[22] Mu2E Collaboration, "Proposal to Search for $\mu^-\mathrm{N} \to e^-\mathrm{N}$ with a Single Event sensitivity Below 10^{-16}", Fermilab, Oct (2008).

[23] K. Ishida, *private communication.*

[24] O. Shanker, Phys. Rev. D **25** 1847 (1982).

[25] R. Watanabe *et al.*, Atomic Data and Nucl. Data Tables **54** 165 (1993).

[26] Y. Miyake, S. Makimura, K. Nishiyama, K. Nagamine, J. Nucl. Mat. **343** 21 (2005).

[27] S. Makimura *et al.*, *Proceedings of the 2nd Annual Meeting of Particle Accelerator Society of Japan and the 30th Linear Accelerator Meeting in Japan*, Tosu, Japan, 20–22 July 2005, 173.

[28] P.A. Piroue and A.J.S. Smith, Phys. Rev. **148** 1315 (1966).

[29] M.G. Catanesi *et al.*, Eur. Phys. J. C 53, 177–204 (2008).

[30] J. Sulkimo *et al.*, Nucl. Instrum. and Methods, Phys. Res. A **506** 250 (2003).

[31] G.f. Cao *et al.*, Nucl. Instrum. and Methods, Phys. Res. A **606** 700 (2009).

[32] A. Bolshakova *et al.*, Eur. Phys. J. C **56** 323 (2008).

[33] A. Aguilar-Arevalo *et al.*, N.I.M. A **609** 102 (2009).

[34] E. Fermi and E. Teller, Phys. Rev. 72 399 (1947).

[35] N.C. Mukhopadhyay, Phys. Rep. **30** 1 (1977).

[36] R. Kitano, M. Koike and Y. Okada, Phys. Rev. D **66** 096002 (2002).

[37] R. Kitano, M. Koike and Y. Okada, Phys. Rev. D **66** 096002 (2002).

[38] V. Cirigliano, R. Kitano, Y. Okada and P. Tuzon, Phys. Rev. D **80** 013002 (2009).

[39] N.T. Zinner, K. Langanke and P. Vogel, arXiv:nucl-th **0606002** (2006).

[40] T. Suzuki, D.F. Measday and J.P. Roalsvig, Phys. Rev. C **35** 2212 (1987).

[41] O. Shanker, Phys. Rev. D **20** 1608 (1979).

[42] G. Newsome *et al.*, J. Nucl. Mat. **371** 76 (2007).

[43] P. Strasser *et al.*, J. Phys: Conf. Series **225** 012050 (2010).

[44] *Muons, Inc.*
http://www.muonsinc.com/tiki-index.php?page=G4beamline

[45] H.A. Enge, Rev. Sci. Instrum. **35** 278 (1964).

[46] J-PARC $(g-2)_\mu$ collaboration, "An Experimental Proposal on a New Measurement of the Muon Anomalous Magnetic Moment $g-2$ and Electric Dipole Moment at J-PARC", KEK J-PARC Proposal (2009).

[47] C. Kost and P.A. Reeve, Lec. Notes Phys. **215** 158 (1984).

[48] M. Hildebrandt for the MEG collaboration, Nucl. Instrum. and Methods, Phys. Res. A **623** 111 (2010)

[49] G. Charpak *et al.*, Nucl. Instrum. and Methods, Phys. Res. A **346** 504 (1994).

[50] P.K. Saha *et al.*, *Proceedings of Hadron Beam 2008*, Nashville, USA, 25–29 August 2008.

[51] Y. Miyake *et al.*, Phys. B **404** 957 (2009).

[52] J. Kamiya *et al.*, IEEE Trans. Appl. Super. **16** 168 (2006).

[53] M. Tomizawa *et al.*, *Proceedings of HB2006*, Tsukuba, Japan (2006).

[54] N. Nakadozono *Master Thesis submitted to Osaka University* (2009).